

**Supplementary Information for:**

**Long-term solar water and CO<sub>2</sub> splitting with  
photoelectrochemical BiOI-BiVO<sub>4</sub> tandems**

Virgil Andrei<sup>1,2†</sup>, Robert A. Jagt<sup>3†</sup>, Motiar Rahaman<sup>1</sup>, Leonardo Lari<sup>4</sup>, Vlado Lazarov<sup>4</sup>, Judith L.  
MacManus-Driscoll<sup>3\*</sup>, Robert L. Z. Hoye<sup>5\*</sup>, and Erwin Reisner<sup>1\*</sup>

<sup>1</sup> *Yusuf Hamied Department of Chemistry, University of Cambridge, Lensfield Road, Cambridge CB2 1EW,  
United Kingdom.*

<sup>2</sup> *Optoelectronics Group, University of Cambridge, Cavendish Laboratory, J J Thomson Avenue,  
Cambridge CB3 0HE, United Kingdom.*

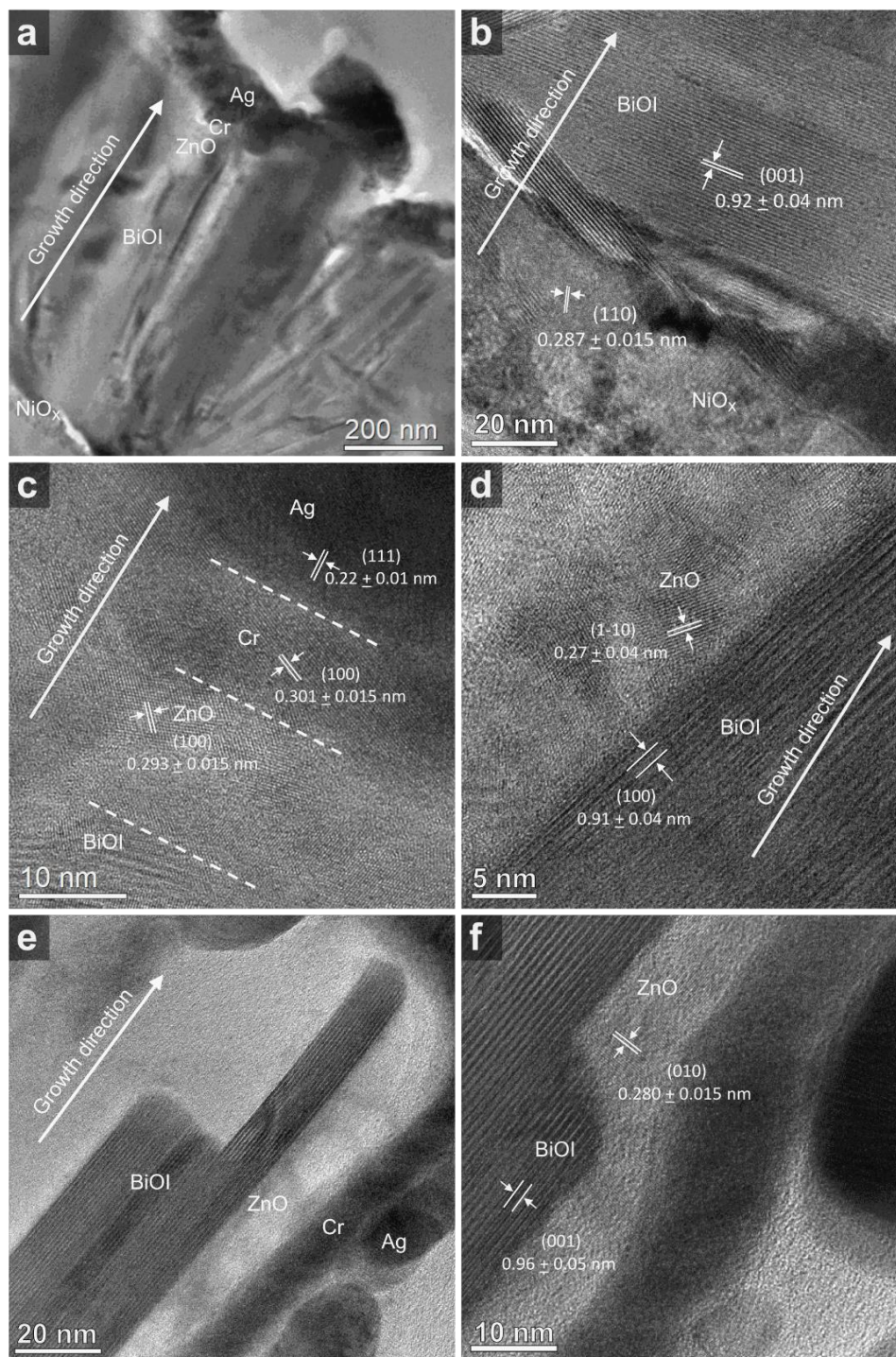
<sup>3</sup> *Department of Materials Science and Metallurgy, University of Cambridge, 27 Charles Babbage Rd,  
Cambridge CB3 0FS, United Kingdom.*

<sup>4</sup> *Department of Physics, University of York, Heslington, York YO10 5DD, United Kingdom.*

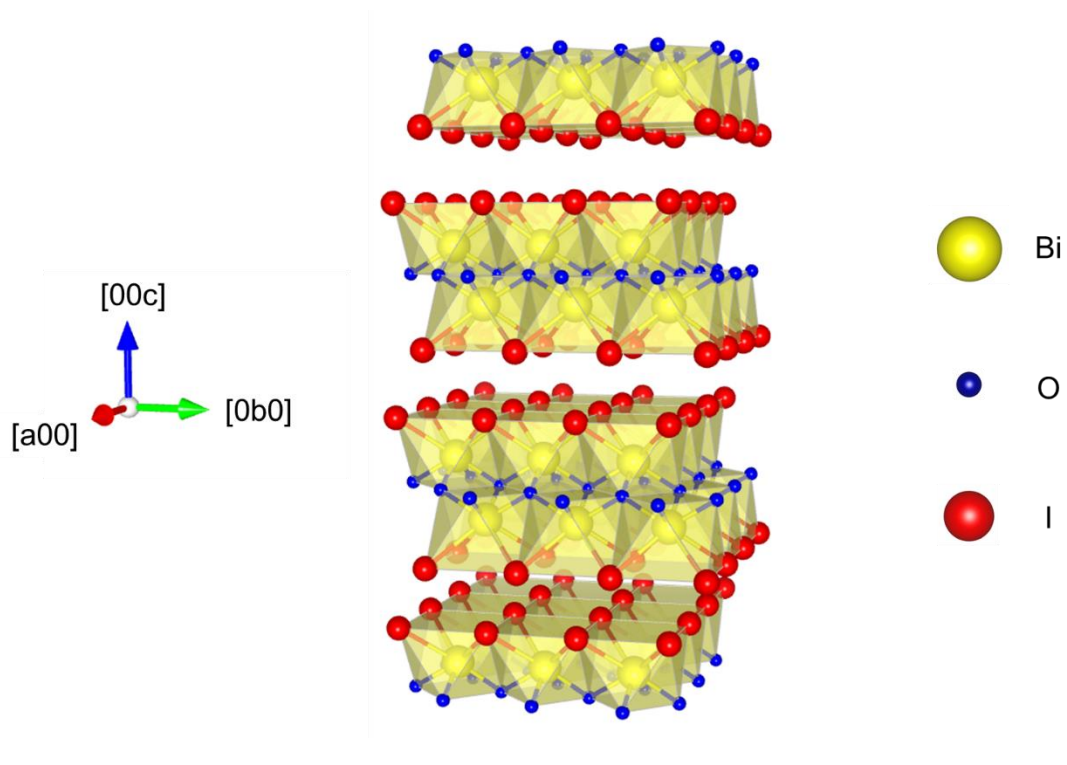
<sup>5</sup> *Department of Materials, Imperial College London, Exhibition Road, London SW7 2AZ, United Kingdom.*

\*Correspondence to: jld35@cam.ac.uk (J.L.M.-D.), r.hoye@imperial.ac.uk (R.L.Z.H.),  
reisner@ch.cam.ac.uk (E.R.).

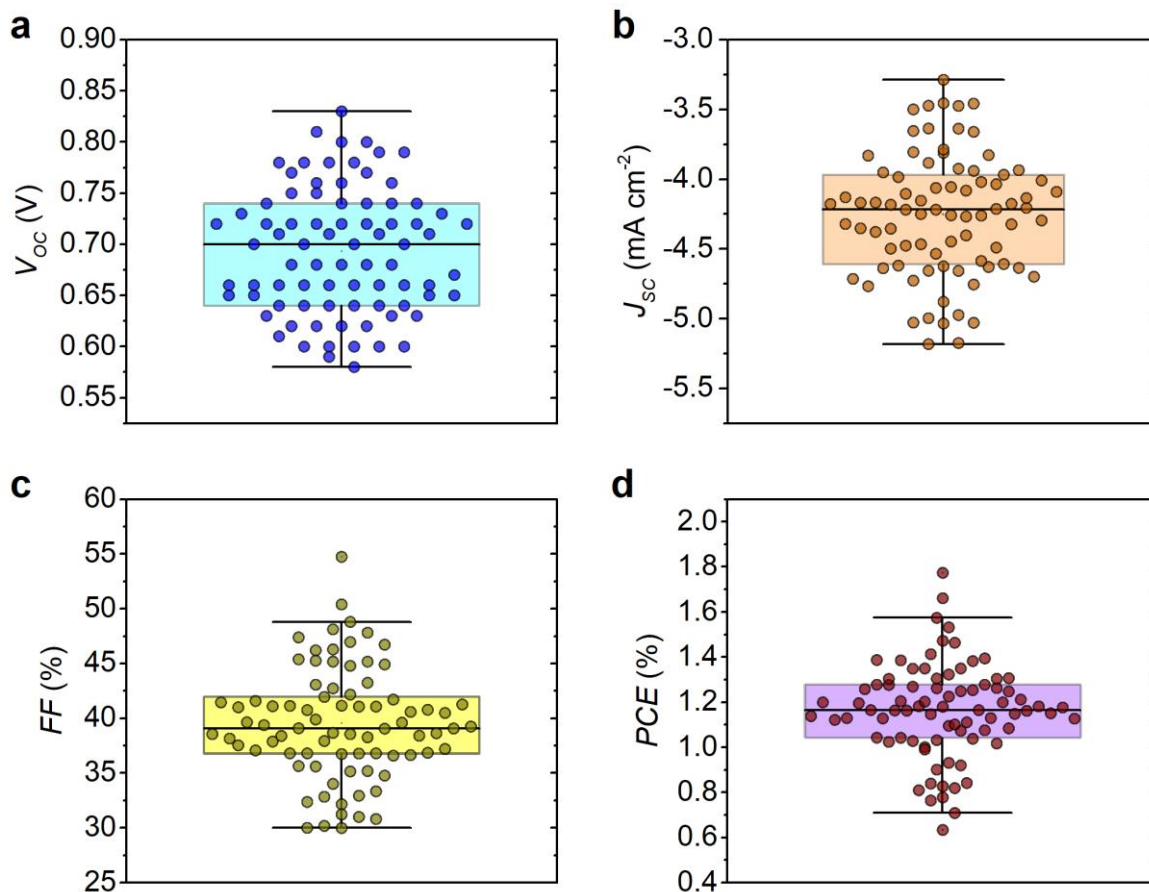
† These authors contributed equally.



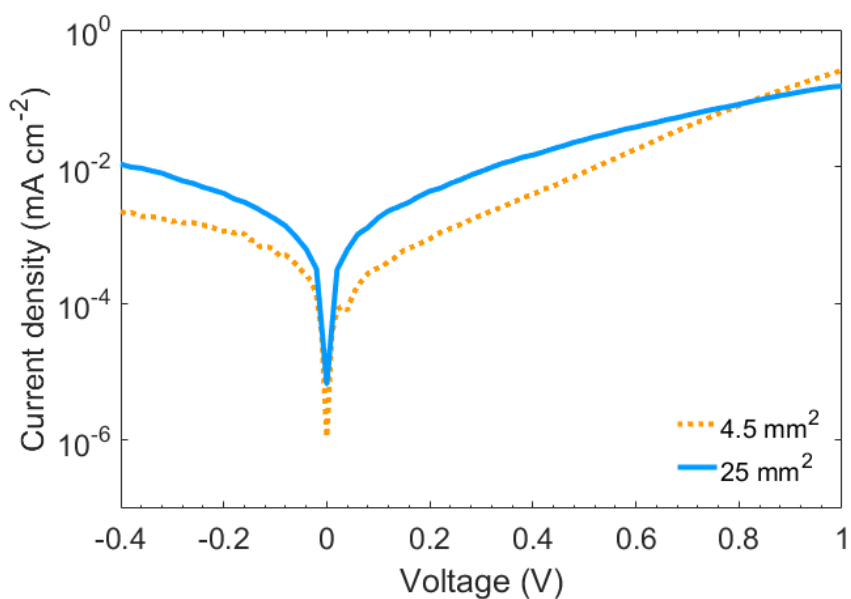
**Supplementary Fig. 1 | TEM images of NiO<sub>x</sub>|BiOI|ZnO|Cr|Ag solar cells on Si substrates.** **a**, Bright field TEM overview image obtained by FIB milling shows the full BiOI PV device structure along the growth direction, including the substrate, NiO<sub>x</sub>, BiOI, ZnO, Cr and Ag contact (n.b. the growth direction denotes the normal to the substrate). **b**, High resolution TEM (HRTEM) image of the interface between the NiO<sub>x</sub> hole transport layer and the BiOI light absorber, revealing the polycrystalline nature of both NiO<sub>x</sub> nanograins and BiOI platelets. The (100) and (110) atomic planes of BiOI and NiO<sub>x</sub> are outlined, respectively. **c**, HRTEM image of the ZnO, Cr and Ag layers. Lattice spacing analysis was used to identify different layers and label characteristic atomic planes. **d**, HRTEM image of the interface between the ZnO electron selective layer and a platelet of BiOI. **e,f**, HRTEM image of a BiOI platelet with the ZnO, Cr and Ag layers. Here it is visible that the ZnO deposited by atmospheric pressure chemical vapor deposition conformally coats the BiOI platelets.



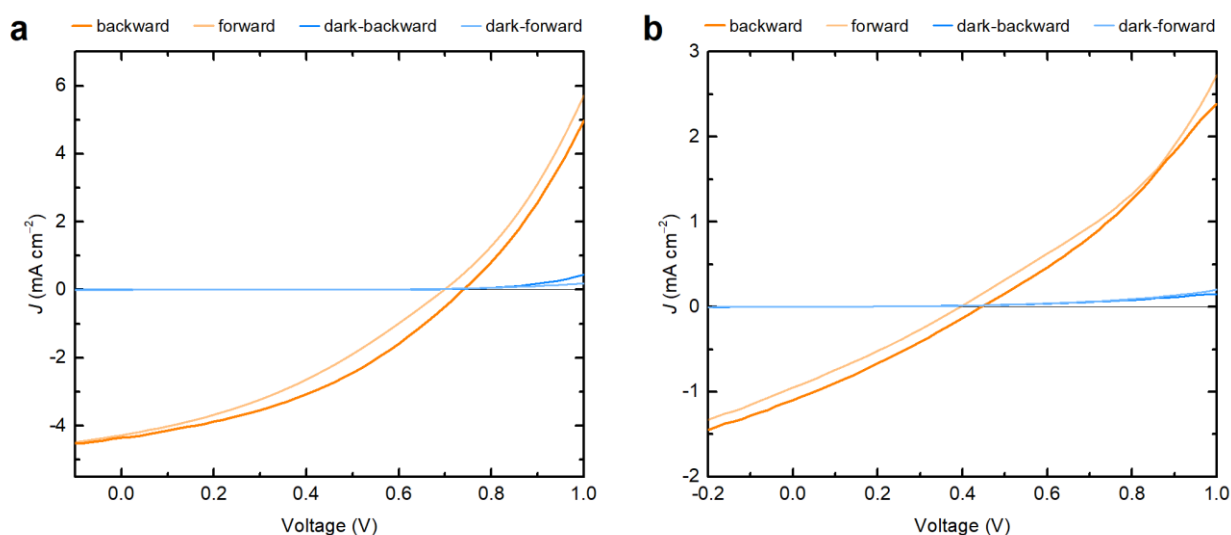
**Supplementary Fig. 2 | Crystal structure of bismuth oxyiodide.** The crystallographic axes are depicted on the left, the labels for the atoms on the right. There are  $3 \times 3 \times 3$  unit cells depicted.



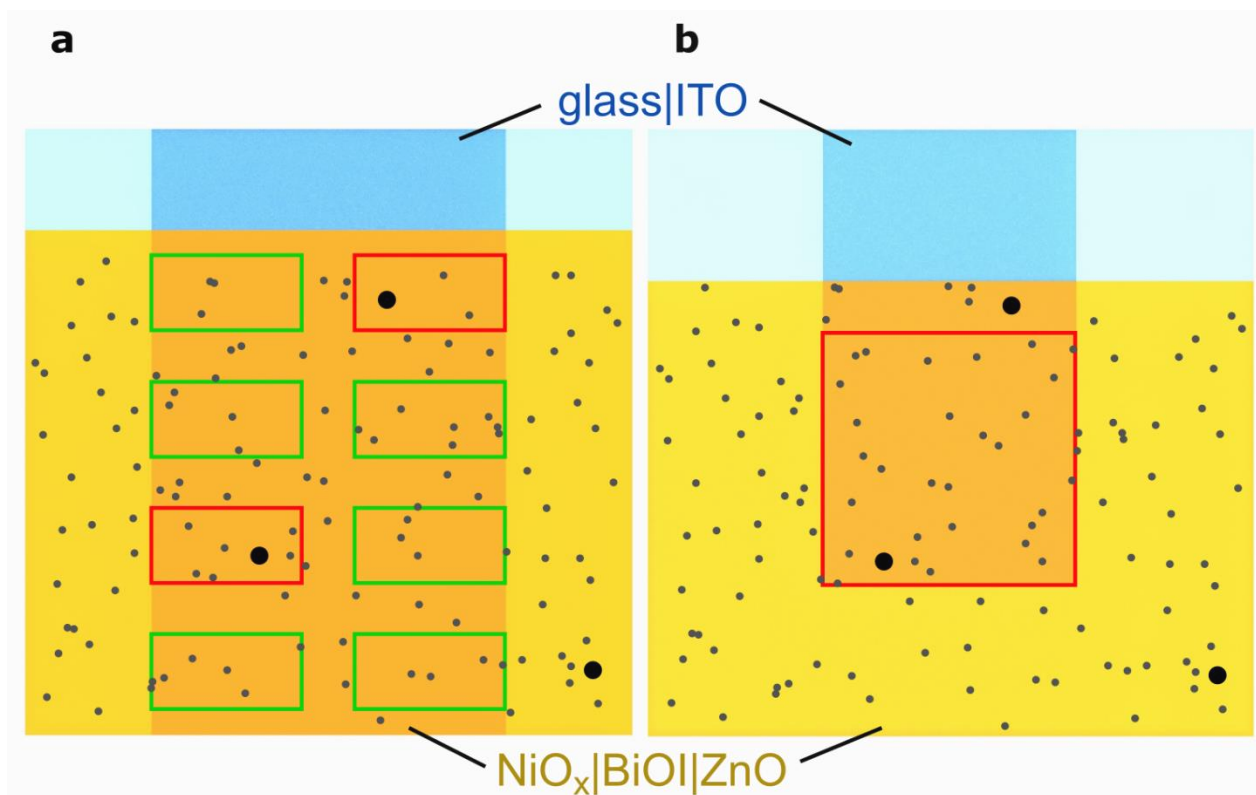
**Supplementary Fig. 3 | Box charts of the photovoltaic parameters for 0.045 cm<sup>2</sup> BiOI devices.** **a**, Open circuit voltage ( $V_{oc}$ ). **b**, Short circuit current density ( $J_{sc}$ ). **c**, Fill factor (FF). **d**, Photovoltaic cell efficiency (PCE). The 81 0.045 cm<sup>2</sup> pixels employed for this study displayed an average  $V_{oc}$  of  $0.69 \pm 0.06$  V,  $J_{sc}$  of  $-4.3 \pm 0.4$  mA cm<sup>-2</sup>,  $40 \pm 5\%$  FF and  $1.2 \pm 0.2\%$  PCE in reverse scan direction. These 81 pixels were deposited on 16 substrates, with 3-7 pixels usually working per substrate. In comparison, 8 single-pixel PV devices with an active area of 0.25 cm<sup>2</sup> only attained an average  $V_{oc}$  of  $0.53 \pm 0.06$  V,  $J_{sc}$  of  $-1.6 \pm 0.3$  mA cm<sup>-2</sup>,  $23 \pm 4\%$  FF and  $0.20 \pm 0.04\%$  PCE in reverse scan direction.



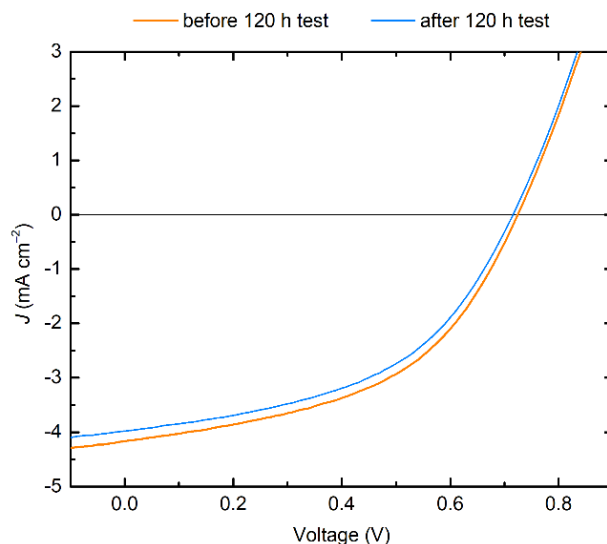
**Supplementary Fig. 4 | Dark current density of two BiOI PV devices.** The active areas are 4.5 mm<sup>2</sup> (yellow dashed line) and 25 mm<sup>2</sup> (blue solid line).



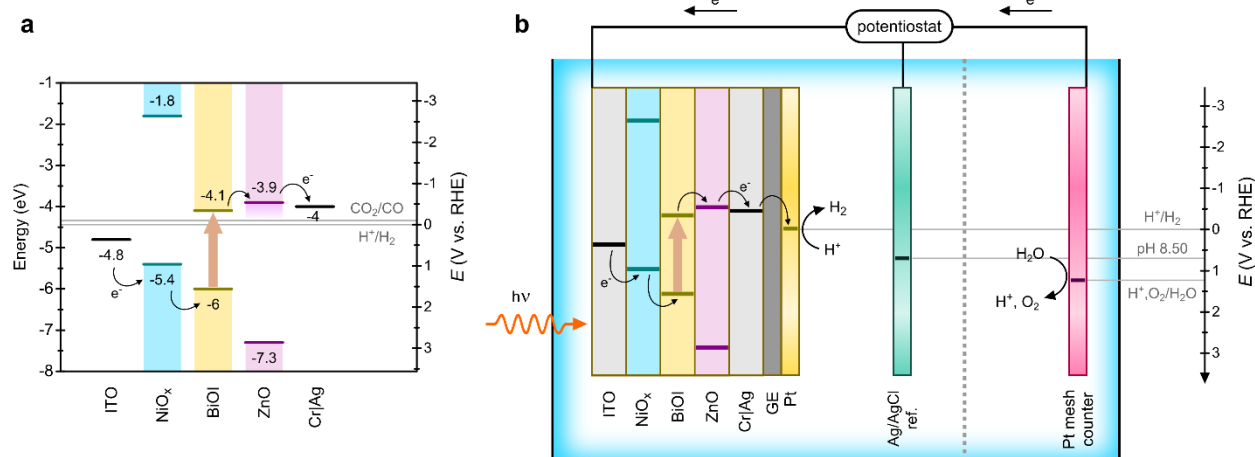
**Supplementary Fig. 5 | Examples of forward and backward  $J$ - $V$  curves for BiOI PV devices of different sizes.** **a**, One representative 0.045 cm<sup>2</sup> pixel from an 8-pixel device. **b**, One-pixel 0.25 cm<sup>2</sup> device. Despite the difference in  $V_{OC}$  and  $J_{SC}$ , the relative hysteresis between forward and backward scans remains similar for both sizes.



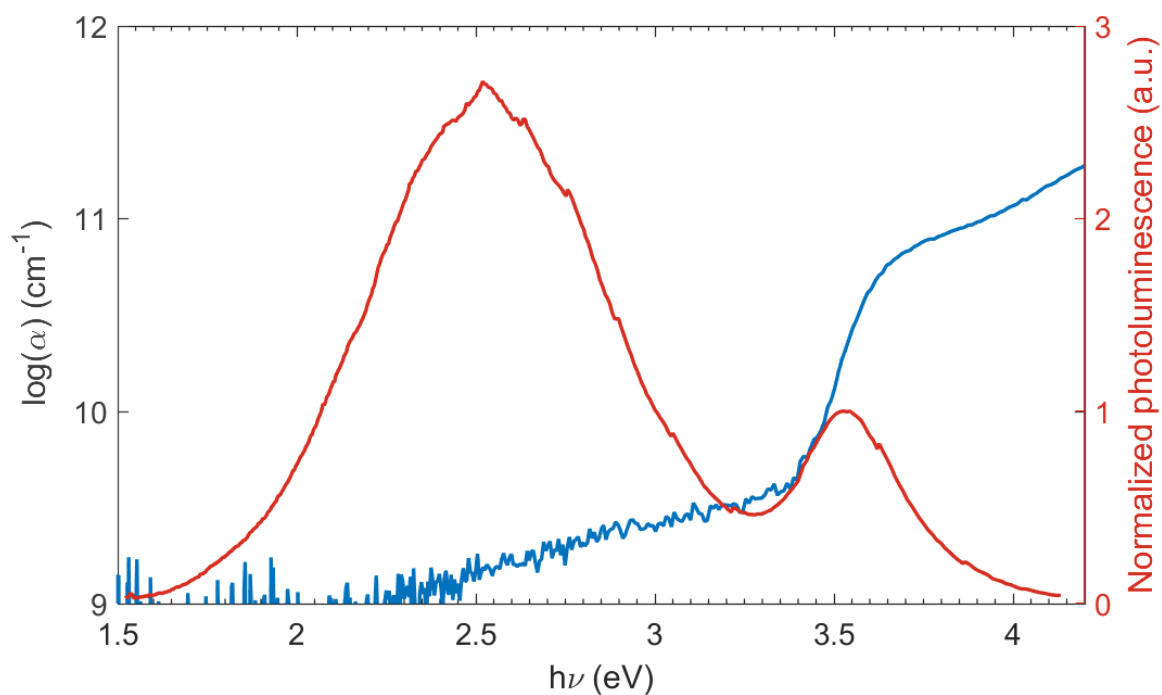
**Supplementary Fig. 6 | Influence of defects and pinholes on the performance of BiOI PV devices.** **a**, 8-pixel device. **b**, Single-pixel PV cell. The same random defect distribution is applied over both BiOI areas. Green contours indicate working pixels, while red margins indicate faulty pixels. Statistically, a  $0.25 \text{ cm}^2$  electrode should contain a 5.6 times higher total number of defects than a  $0.045 \text{ cm}^2$  pixel. Qualitatively, we can differentiate between two types of defects: small defects that decrease the pixel performance (depicted as randomly distributed grey dots), and large defects which damage the entire device structure (black circles). In case of smaller defects, these only contribute to a decrease in photovoltage and photocurrent (i.e. shunting losses), which can be seen from the difference between the  $V_{oc}$  and  $J_{sc}$  of  $0.045$  and  $0.25 \text{ cm}^2$  pixel PV devices (see Fig. 1e). This effect has been often observed across different photovoltaic technologies (e.g. perovskite solar cells), as the performance decreases with increasing active area. In contrast, there is a higher probability of encountering a major defect over a larger area, which will damage the entire active area, causing a shorted device. In practice, at least 3 pixels were functional on each 8-pixel substrate, whereas only one out of 3-4 single-pixel BiOI samples deposited on individual substrates was typically working. This provides a practical challenge for large-scale production, as even one major defect can short the entire device resulting in a higher number of faulty devices, i.e. higher material waste.



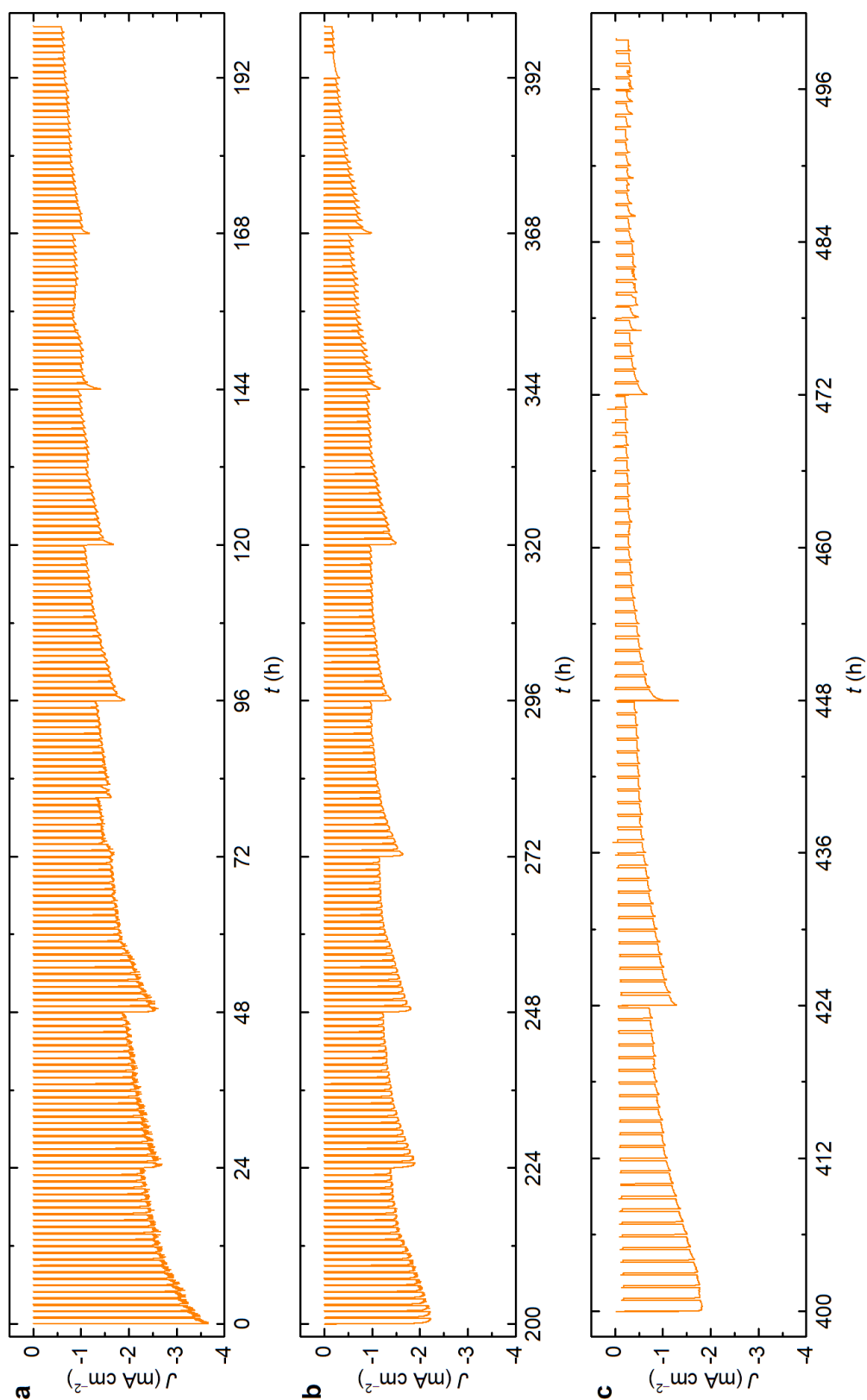
**Supplementary Fig. 7 | J-V curves of a BiOI PV device before and after a long-term stability test.** A  $0.045 \text{ cm}^2$  PV cell was continuously irradiated for 125 h, at 0.55 V bias (the corresponding long-term photocurrent trace is given in Fig. 1h from the main text). The device displayed a  $V_{OC}$  of 0.73 V,  $J_{SC}$  of  $-4.17 \text{ mA cm}^{-2}$ , 48.1% FF and 1.46% PCE before, and a  $V_{OC}$  of 0.72 V,  $J_{SC}$  of  $-3.98 \text{ mA cm}^{-2}$ , 47.9% FF and 1.37% PCE after the 125 h test, in backward scan direction. The negligible change in  $V_{OC}$  and minor decrease in  $J_{SC}$  revealed an encouraging stability for the BiOI PV system.



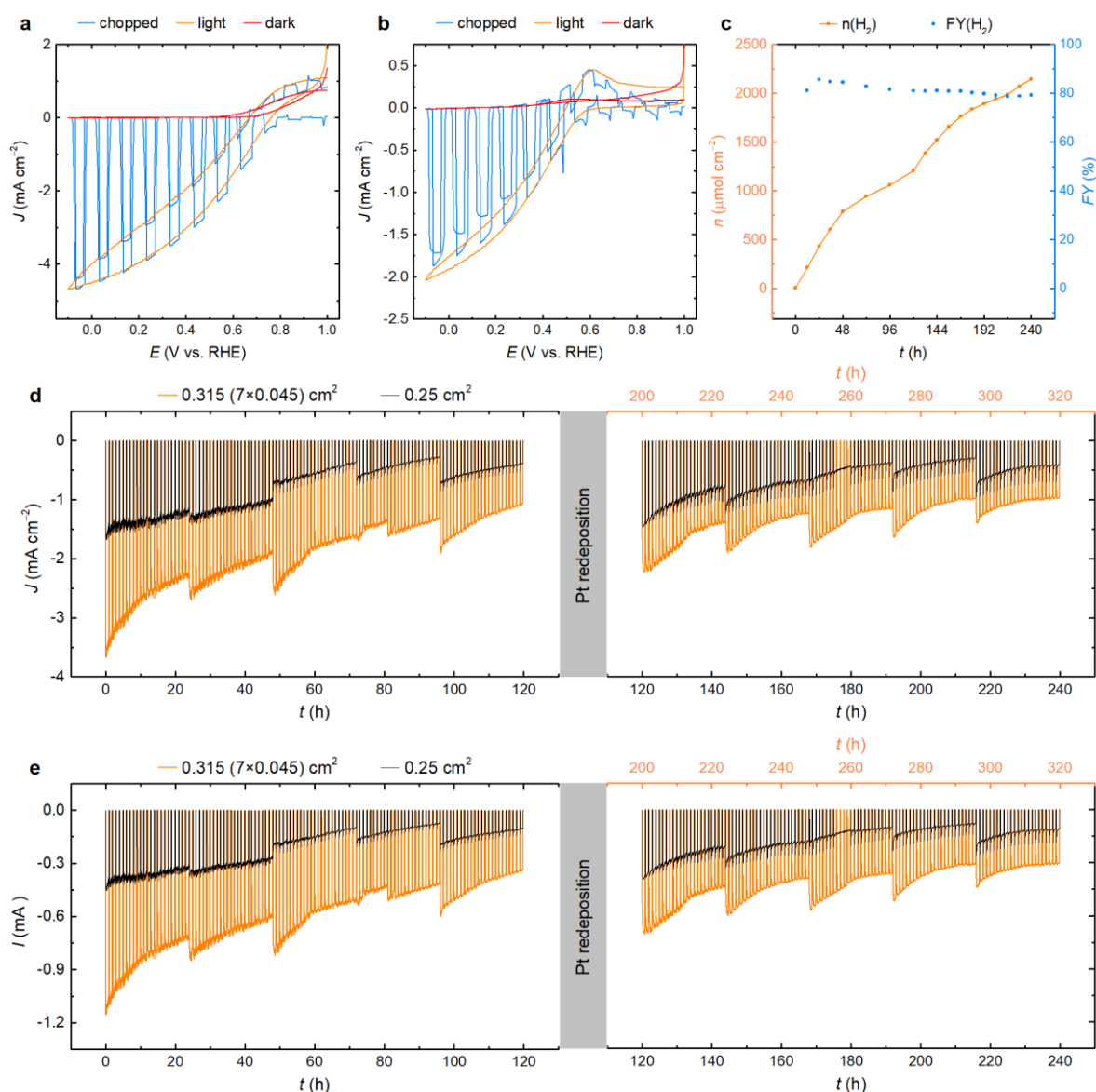
**Supplementary Fig. 8 | Band structures of the BiOI PV cells and photocathodes.** **a**, Energy levels within a BiOI PV device. **b**, Schematic of the energy levels of a BiOI photocathode in solution, wired in a three-electrode configuration with a Ag/AgCl/NaCl(sat.) reference electrode, and a Pt mesh counter electrode. Owing to its intrinsic nature, BiOI has a low carrier concentration and therefore will have a large depletion width when deposited onto *n*- or *p*-type substrates. When BiOI is sandwiched between NiO<sub>x</sub> and ZnO a built-in potential is created, which under short-circuit conditions cause electrons to get injected into the ZnO and directed towards the Cr|Ag contact. Whilst the electron affinity of ZnO is lower than that of BiOI, electrons can still be injected into the tail of states extending from the conduction band minimum of ZnO and into the bandgap, meaning that there is no extraction barrier (see absorption and photoluminescence spectra of ZnO in Supplementary Fig. 9). These electrons are transferred through the conductive graphite epoxy (i.e. ohmic contact) to either a Pt or Cu<sub>2</sub>In<sub>8</sub> catalyst. The BiOI photocathode is therefore capable of both hydrogen evolution and CO<sub>2</sub> reduction.



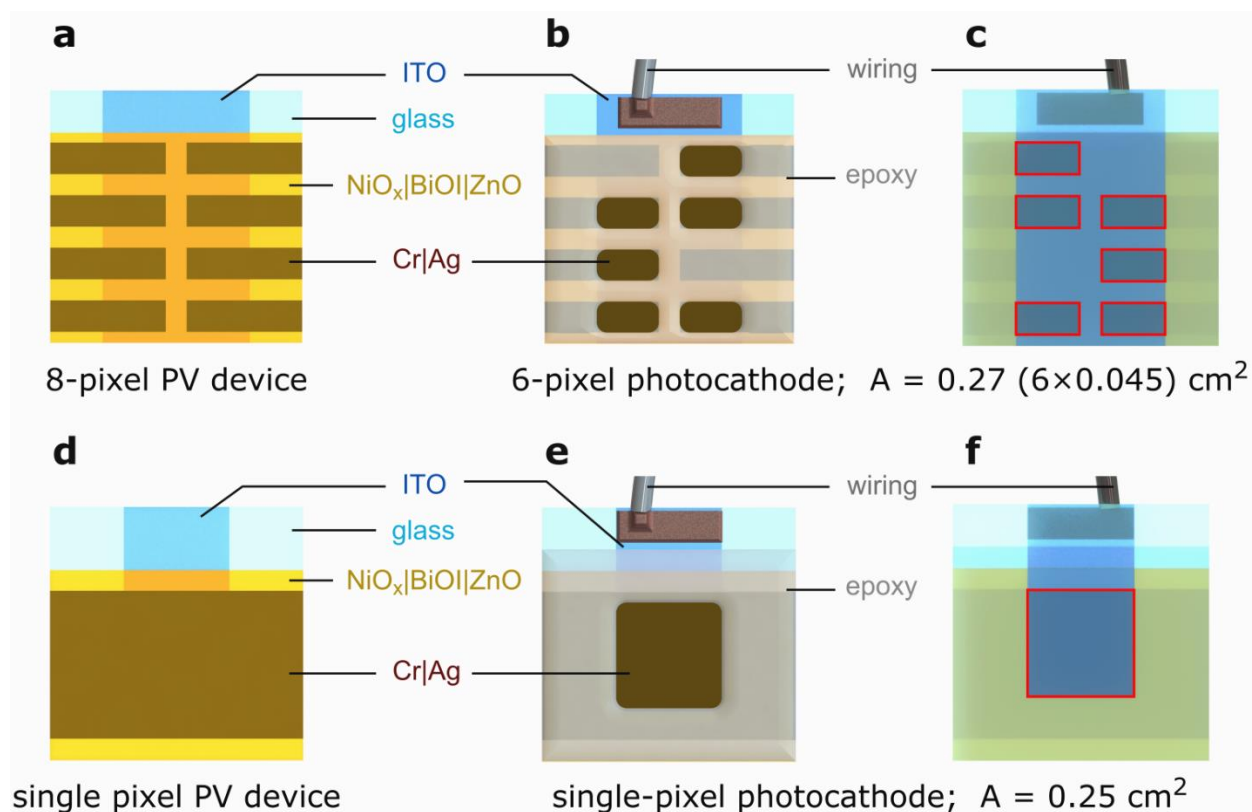
**Supplementary Fig. 9 | Absorption and photoluminescence (PL) spectra of ZnO.** The ZnO films grown here were deposited at a low temperature of 80 °C, and therefore have many defects and high levels of disorder. This results in a high density of tail states extending from the band-edges. Charges can be injected into these tail states. In our case, electrons from BiOI can be injected 0.3 eV below the conduction band minimum, where the density of electron acceptor states is sufficient to sustain photocurrents without presenting a charge extraction barrier<sup>1</sup>. Figure adapted with permission from Ref. 2.



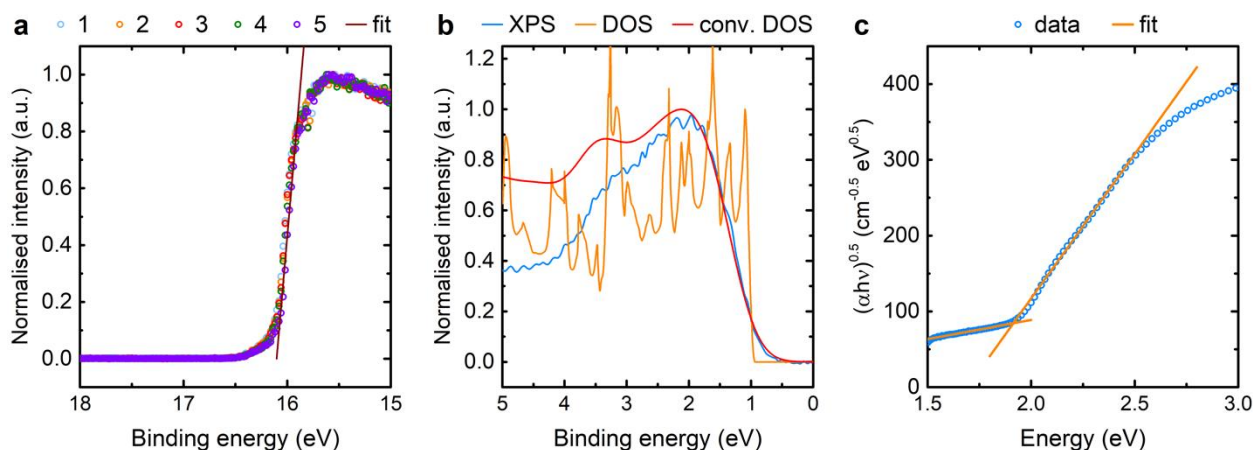
**Supplementary Fig. 10 | Close-up view of the photocurrent trace during the 500 h stability test of a BiOI photocathode at 0 V vs. RHE.** The three plots depict the hours under operation following the Pt catalyst (re)deposition. **a**, 0-200 h. **b**, 200-400 h. **c**, 400-500 h. Chronoamperometry was performed under simulated solar irradiation ( $\text{AM 1.5G}$ ,  $100 \text{ mW cm}^{-2}$ ), in a  $0.1 \text{ M KBi}$ ,  $0.1 \text{ M K}_2\text{SO}_4$  electrolyte solution, pH 8.50, under  $\text{N}_2$ , at room temperature.



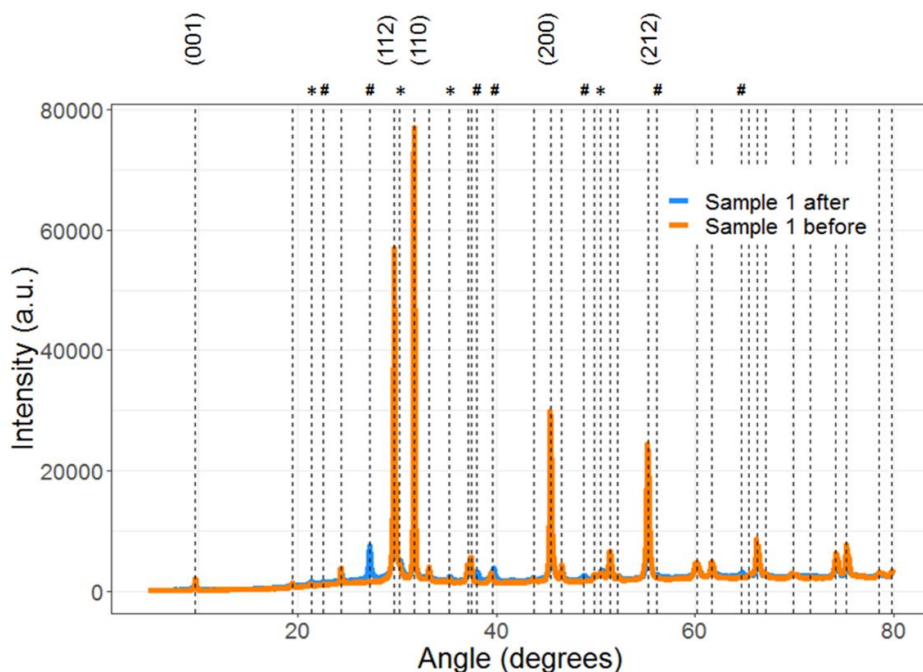
**Supplementary Fig. 11 | Photoelectrochemical characterization of the BiOI|GE|Pt photocathodes.** **a**, Cyclic voltammetry (CV) scans of a photocathode consisting of seven  $0.045 \text{ cm}^2$  working BiOI pixels (i.e.  $0.315 \text{ cm}^2$  photoactive area) under chopped, continuous and no light irradiation. **b**, CV scans of a  $0.25 \text{ cm}^2$  one-pixel photocathode. **c**, Close-up of the  $\text{H}_2$  evolution over time for the  $0.25 \text{ cm}^2$  electrode. **d**, Comparison of the photocurrent decay over time and recovery after Pt redeposition for the  $0.315 (7 \times 0.045) \text{ cm}^2$  and  $0.25 \text{ cm}^2$  photocathodes. While the absolute decay rates are comparable, the relative decrease in photocurrent is higher for the  $0.25 \text{ cm}^2$  photocathode due to its smaller photocurrent density. A partial recovery in respect to the initial photocurrent is observed in both cases ( $7 \times 0.045$  and  $0.25 \text{ cm}^2$ ) when redepositing  $5 \text{ nm}$  Pt, irrespective of the prior operation time (200 vs. 120 h), or resting time in between long-term tests (21 vs. 0 days, respectively). Experiments are conducted under simulated solar irradiation (AM 1.5G,  $100 \text{ mW cm}^{-2}$ ), in  $0.1 \text{ M KBi}$ ,  $0.1 \text{ M K}_2\text{SO}_4$ , pH 8.50, under  $\text{N}_2$ , at room temperature. **e**, Absolute photocurrents for the two photocathodes described in frame **d**. The  $0.315 (7 \times 0.045) \text{ cm}^2$  photocathode presents a roughly 2.5 times higher absolute photocurrent than a  $0.25 \text{ cm}^2$  single pixel electrode, even though both devices are fabricated on substrates of the same total area ( $1.2 \times 1.2 \text{ cm}^2$ ). Hence, the photocurrent of multiple-pixel devices also surpasses single-pixel electrodes when considered over the entire device area.



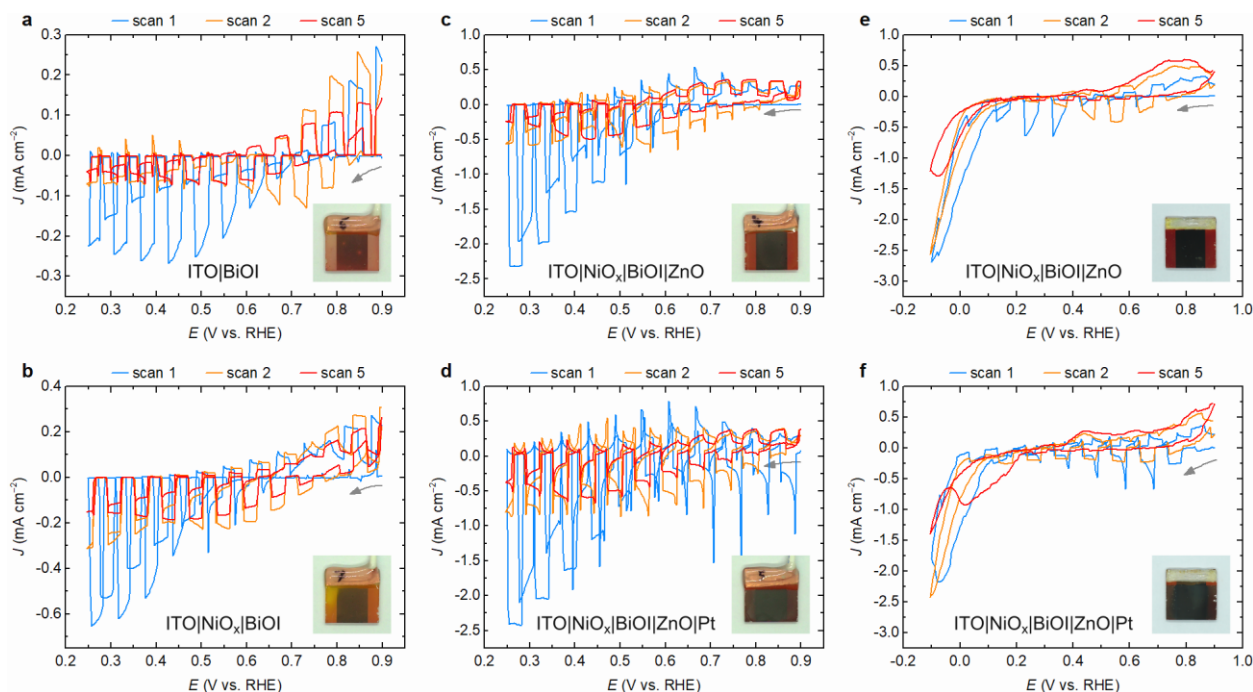
**Supplementary Fig. 12 | Photoactive areas for different PV and PEC pixel arrangements.** **a,b,c**, Multiple-pixel arrangement. **d,e,f**, Single-pixel design. **a,d**, PV devices. **b,c,e,f**, Partially encapsulated photocathodes, seen from: **b,e** - the front side, **c,f** - the back side (corresponding to the images in Supplementary Fig. 40a,b). In case of the multiple-pixel arrangement, eight independently working,  $0.045 \text{ cm}^2$  PV cells are defined by evaporating metal Cr/Ag contacts onto a  $1.2 \times 1.2 \text{ cm}^2$  substrate through a mask. Each substrate forms the basis for a multiple-pixel photocathode. In example **b**, six working pixels are selected for the photocathode, whereas two faulty pixels and the remaining non-active area are sealed by epoxy. The six working pixels are connected in parallel via the conductive graphite epoxy paste (see Supplementary Fig. 40b,d), resulting in an electrode with a total photoactive area of  $6 \times 0.045 \text{ cm}^2 = 0.27 \text{ cm}^2$  (see red highlights). In this multiple-pixel arrangement, the photocathode maintains the higher voltage of the small-area pixels, while the absolute photocurrents add up (i.e. the overall photocurrent density remains similar). In contrast, only one  $0.25 \text{ cm}^2$  PV cell is deposited on the  $1.2 \times 1.2 \text{ cm}^2$  substrate in case of the single-pixel devices, with its photoactive area defined by the size of the conductive ITO stripe (see **f**). The non-active area is again sealed by epoxy when assembling the photocathode.



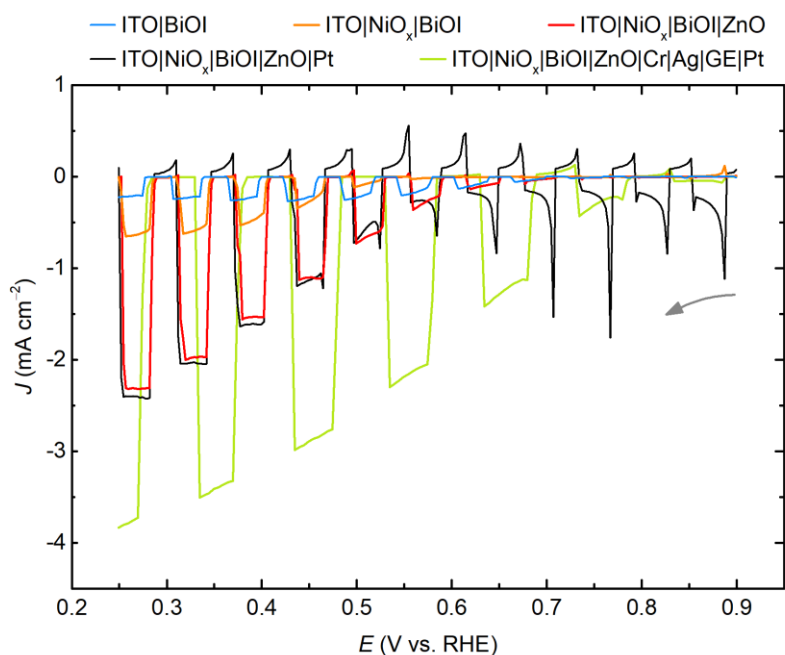
**Supplementary Fig. 13 | Spectroscopic determination of the BiOI band structure.** **a**, Ultraviolet photoelectron spectroscopy (UPS). **b**, Density of states (DOS) convolved with a Gaussian representing instrument broadening, overlaid onto the measured X-ray photoelectron spectroscopy (XPS) data (adapted with permission from Ref. 2). **c**, UV-vis data indicating the bandgap of BiOI. Previous photoemission spectroscopy measurements revealed that the BiOI employed here is near-intrinsic. This is in agreement with defect calculations made on BiOI, in which the cross-over point between the lowest formation energy donor and acceptor defects is in the middle of the band gap. In fact, BiOI is a self-compensating system, in which the formation of donor defects will lead to the formation of compensating acceptor defects to keep the Fermi level mid-gap, with a VB to Fermi-level offset of  $0.95 \pm 0.15$  eV. The band extrema of the 720 nm thick BiOI film deposited on ITO|NiO<sub>x</sub> are -4.1 eV (conduction band minimum) and -6.0 eV (valence band maximum), which are -0.34 V (RHE) and 1.56 V (RHE), respectively<sup>2,3</sup>.



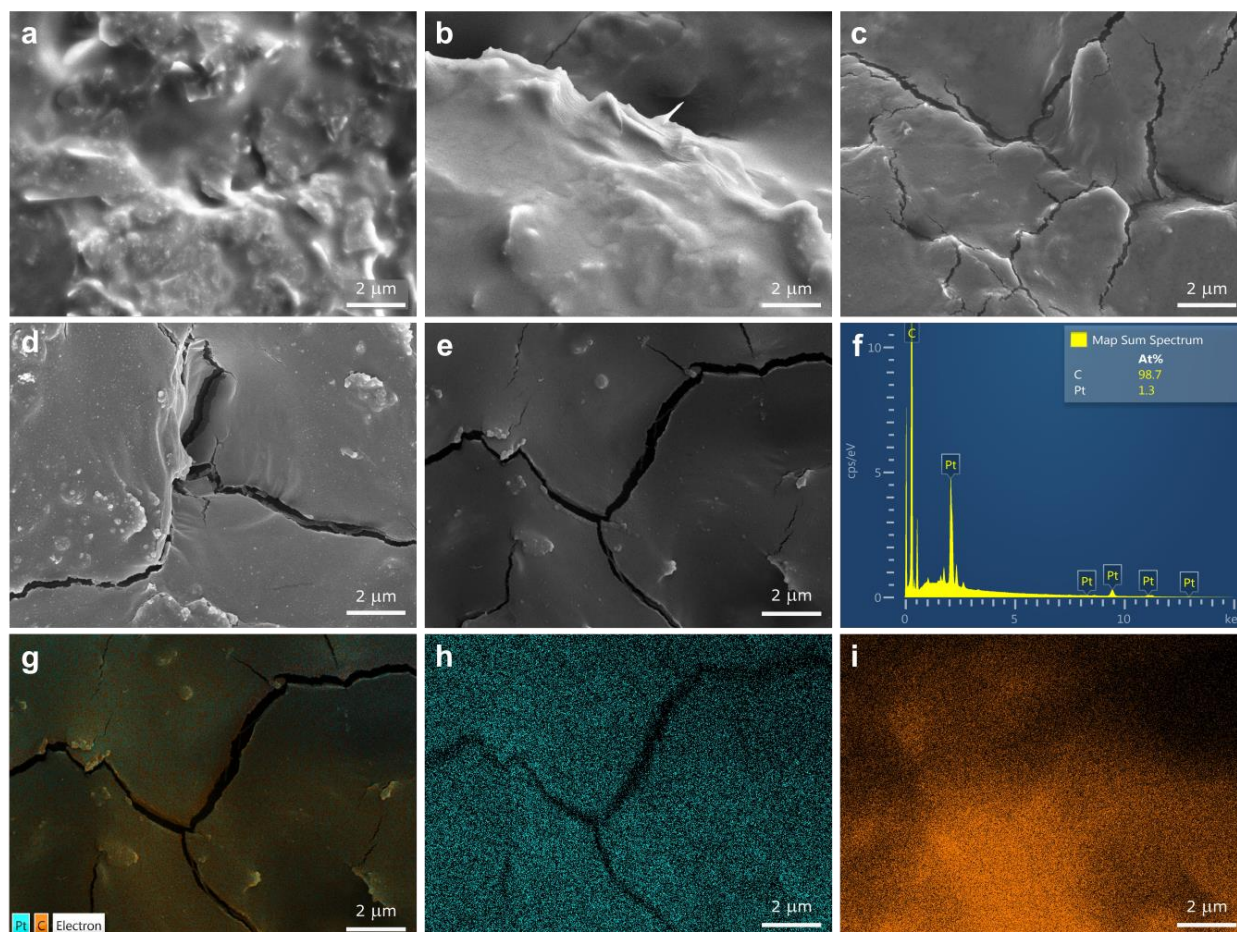
**Supplementary Fig. 14 | X-ray diffraction (XRD) pattern of bismuth oxyiodide.** XRD pattern before (orange) and after (blue) usage as a non-encapsulated ITO|NiO<sub>x</sub>|BiOI|ZnO photocathode in an aqueous solution (see details in Supplementary Fig. 15). The vertical dotted lines indicate identified peak positions. An \* indicates a peak position due to the ITO substrate, while # indicate peak positions corresponding to metallic bismuth. The Miller indices of the dominant peaks are indicated on top of the graph.



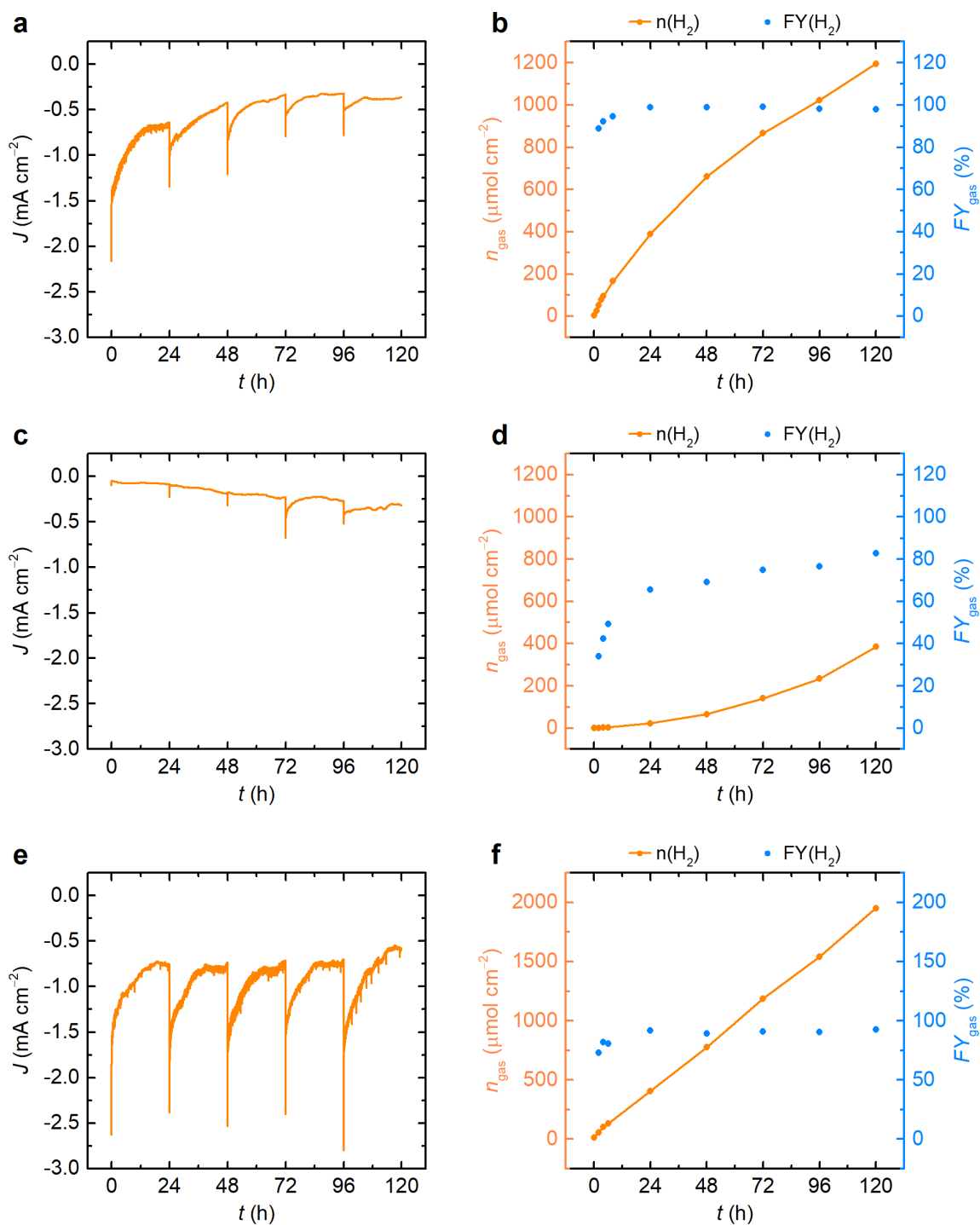
**Supplementary Fig. 15 | Photoelectrochemical characterization of unprotected BiOI photocathodes. a,** CVs of a bare ITO|BiOI photocathode. **b,** CVs of ITO|NiO<sub>x</sub>|BiOI. **c,e,** CVs of ITO|NiO<sub>x</sub>|BiOI|ZnO. **d,f,** CVs of ITO|NiO<sub>x</sub>|BiOI|ZnO|Pt. **a-d** – CVs are scanned between 0.9 and 0.25 V vs. RHE, with light chopped in 3 s on, 3 s off cycles. **e,f** – CVs are scanned between 0.9 and -0.1 V vs. RHE, with light chopped in 5 s on, 5 s off cycles. Grey arrows indicate the scan start and direction. Insets show the change in color of the photocathodes after 5 CV cycles (10 mV s<sup>-1</sup> scan rate), which can be assigned to a partial BiOI reduction to a metallic Bi phase (see Supplementary Fig. 14). This change is only observed for BiOI deposited above the patterned ITO stripe. Similar degradation patterns are observed both in the presence and absence of the 5 nm Pt layer, indicating that the Bi reduction is not caused by insufficient charge extraction / charge accumulation. An increased dark current can be observed in frames **e** and **f**, as BiOI electroreduction occurs at applied potentials below 0.2 V vs. RHE. The photocurrent was significantly diminished over subsequent scans for all samples, as BiOI reduction occurred during the first CV cycle (see Supplementary Movie 2). No H<sub>2</sub> was detected over the five cycles for samples in **a-d**, which indicates the photocurrent is solely caused by BiOI reduction. An anodic photocurrent was only observed after the BiOI reduction over the first scan (Supplementary Fig. 16), which indicates the current is due to Bi reoxidation. CVs were conducted under chopped light irradiation (AM 1.5G, 100 mW cm<sup>-2</sup>), in 0.1 M KBi, 0.1 M K<sub>2</sub>SO<sub>4</sub>, pH 8.50, under N<sub>2</sub>, at room temperature.



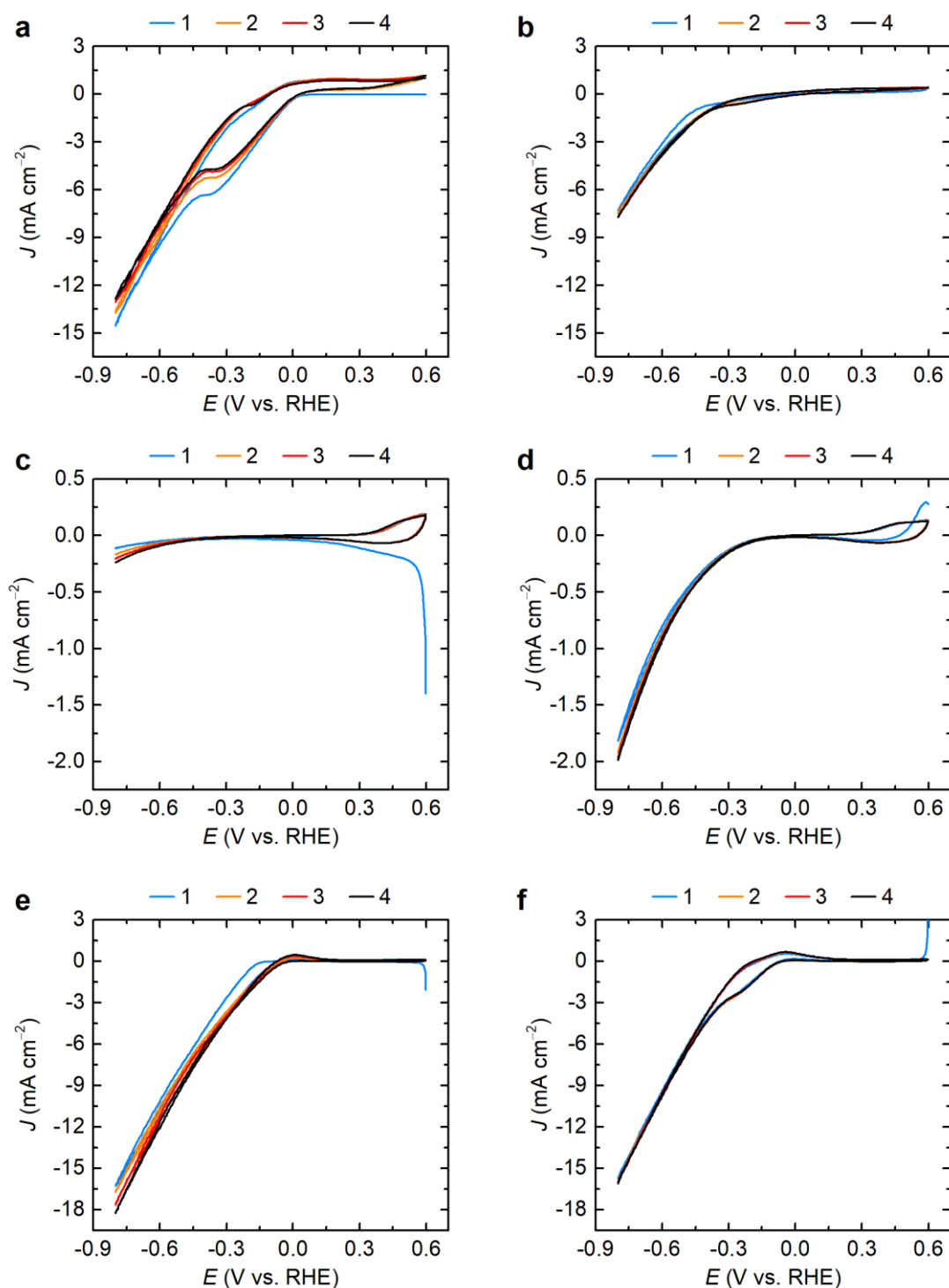
**Supplementary Fig. 16 | Comparison between the initial photocurrents of unprotected BiOI photocathodes.** Plot depicts the initial forward scans of the samples described in Supplementary Fig. 15. An ITO|BiOI electrode displayed the lowest photocurrent. Photocathodes with both NiO<sub>x</sub> and ZnO charge selective layers displayed similar photocurrents with or without a Pt layer, as the photocurrent was due to BiOI reduction (see Supplementary Fig. 15). No anodic photocurrent was observed when scanning the unprotected, ~0.5 cm<sup>2</sup> photocathodes from 0.9 to 0.25 V vs. RHE. For comparison, a graphite epoxy encapsulated, 0.315 (7×0.045) cm<sup>2</sup> photocathode displayed a higher photocurrent density and onset potential for H<sub>2</sub> evolution. The beneficial effect of adding hole and electron selective layers is well established from the PV community, as a significant increase in the performance of BiOI PV cells has been reported by carefully designing the device structure<sup>2</sup>. These findings indicate that the complete buried PV photocathode structure, including the conductive encapsulant, is required to obtain practical solar fuel production.



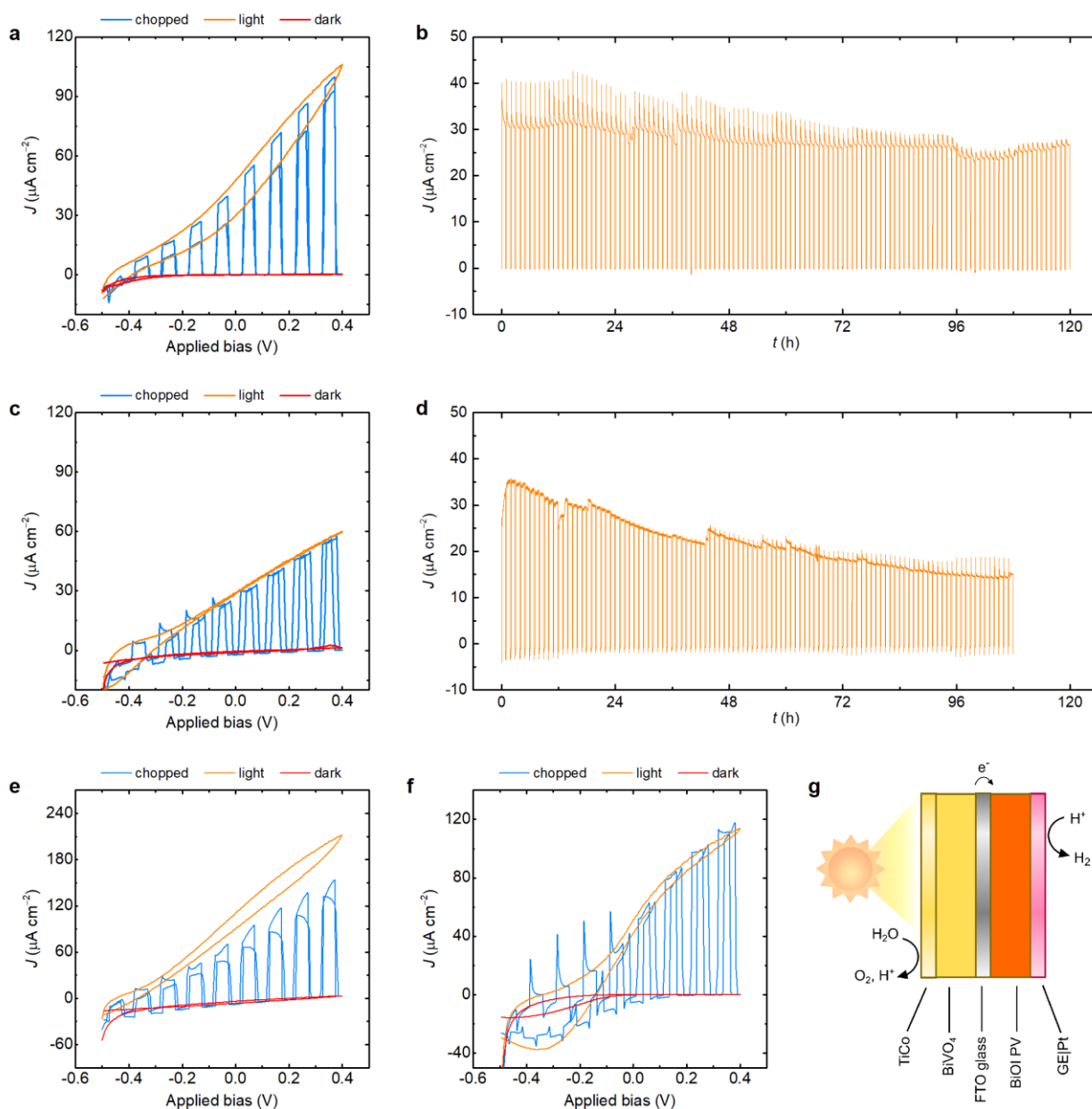
**Supplementary Fig. 17 | Degradation of the GE|Pt electrocatalyst surface over the 500 h BiOI|GE|Pt photocathode test. a-e**, SEM images. **a**, Pristine GE surface. **b**, Fresh GE|Pt electrocatalyst. **c**, GE|Pt catalyst after a 120 h electrolysis test (Supplementary Fig. 18a). **d,e**, GE|Pt surface after the 500 h photocathode test (Fig. 2b, main text). **f**, EDX spectrum corresponding to the area depicted in frame **e**. **g-i**, Overall (**g**), platinum (**h**) and carbon (**i**) elemental mapping. As observed previously, a decrease in activity of the Pt catalyst is caused by nano-cracks forming over the GE|Pt catalyst interface which may affect the electronic transport, whereas only a minimal amount of Pt (below 1%) becomes detached from the electrode surface<sup>4</sup>.



**Supplementary Fig. 18 | Long-term stability tests of H<sub>2</sub> evolution electrocatalysts.** **a,b**, GE|Pt (at -0.2 V vs. RHE). **c,d**, GE|RuO<sub>x</sub> (-0.5 V vs. RHE). **e,f**, FTO|RuO<sub>x</sub> (-0.2 V vs. RHE). **a,c,e**, Long-term chronoamperometric trace. **b,d,f**, Corresponding cumulative product amounts and faradaic yield (FY). A similar daily decay can be reverted for both GE|Pt and FTO|RuO<sub>x</sub> by changing the 0.1 M KBi, 0.1 M K<sub>2</sub>SO<sub>4</sub>, pH 8.50 electrolyte solution and repurging it with N<sub>2</sub> every 24 h. An additional gradual decay of the catalyst is observed for platinum. However, the GE-electrodeposited RuO<sub>x</sub> showcases low current densities even at a more negative applied potential (see also Supplementary Fig. 19).

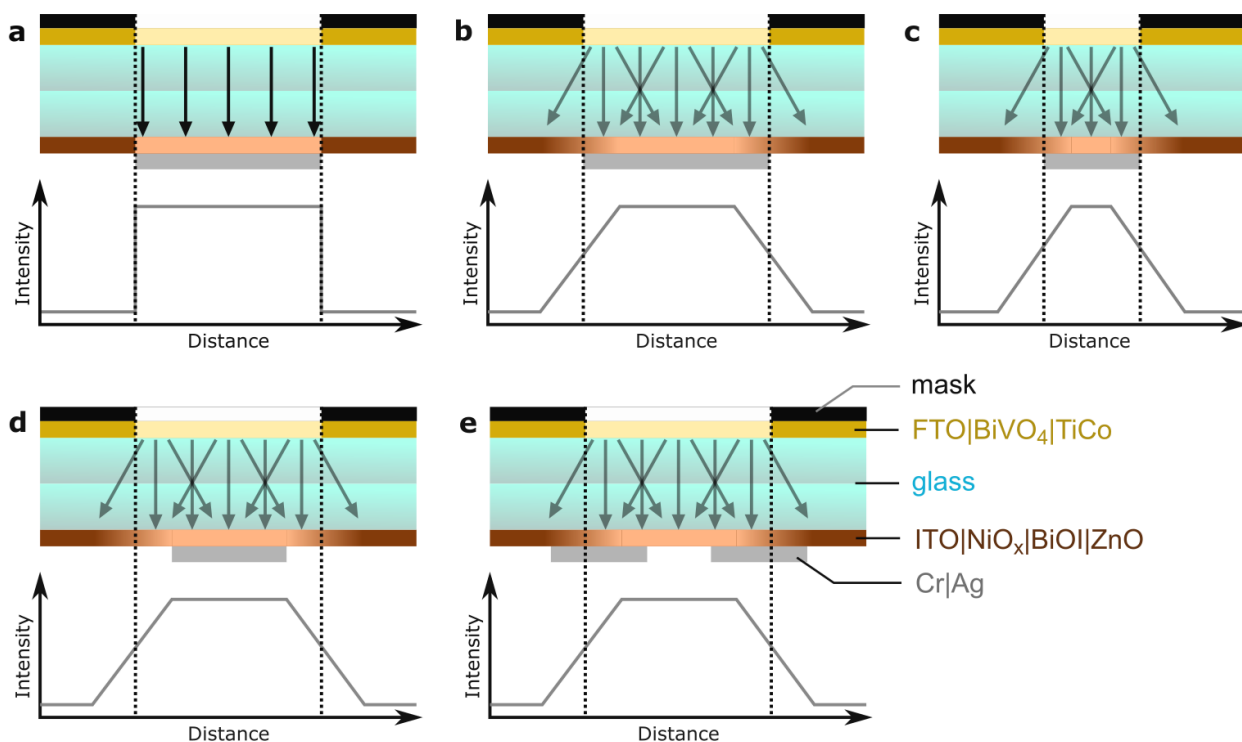


**Supplementary Fig. 19 | Cyclic voltammetry scans of the investigated H<sub>2</sub> evolution electrocatalysts. a,b,** GE|Pt. **c,d,** GE|RuO<sub>x</sub>. **e,f,** FTO|RuO<sub>x</sub>. CV scans are recorded before (**a, c, e**) and after (**b, d, f**) long-term stability tests in 0.1 M KBi, 0.1 M K<sub>2</sub>SO<sub>4</sub>, pH 8.50, under N<sub>2</sub>. A higher overpotential for H<sub>2</sub> evolution is observed for both GE|Pt and FTO|RuO<sub>x</sub>, whereas an increase in current is observed for the GE|RuO<sub>x</sub> after the long-term test.



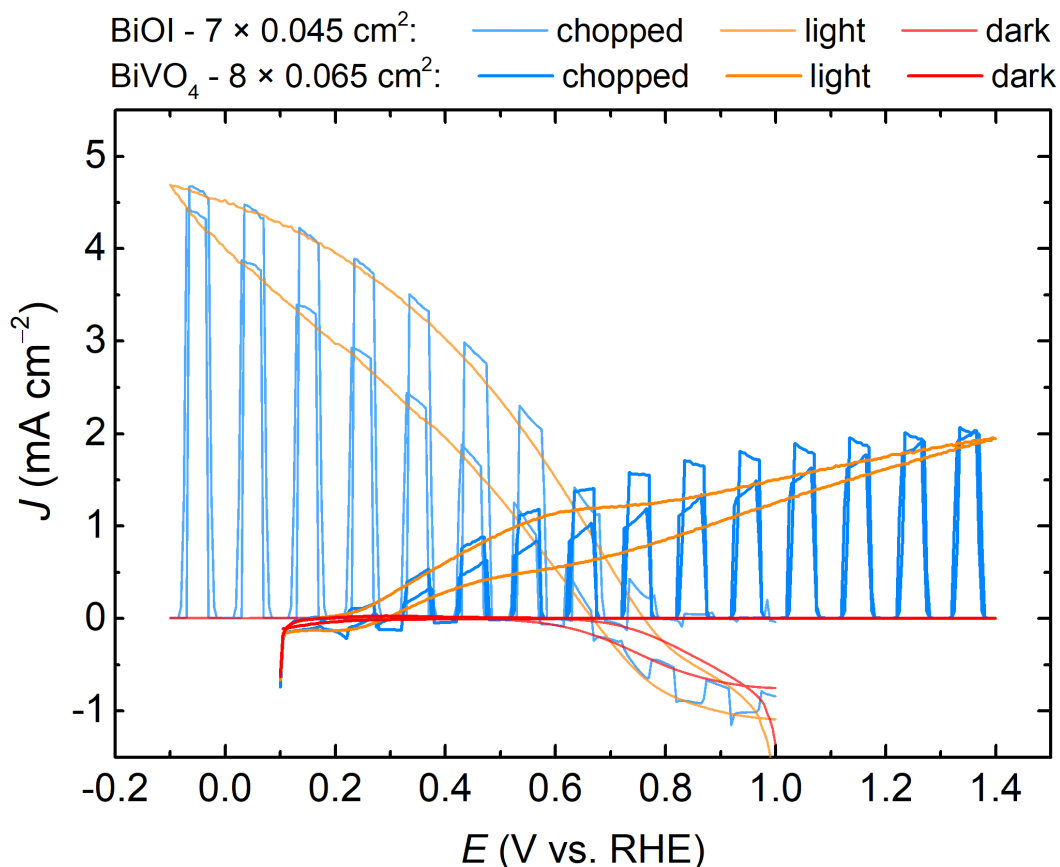
**Supplementary Fig. 20 | Performance of BiOI|GE|Pt - BiVO<sub>4</sub> tandem devices in different configurations.**

**a,b**,  $0.27 (6 \times 0.045) \text{ cm}^2$  BiOI -  $0.27 (6 \times 0.045) \text{ cm}^2$  BiVO<sub>4</sub> (i.e. ideal geometric overlap between the BiVO<sub>4</sub> and BiOI active areas). **c,d**,  $0.225 (5 \times 0.045) \text{ cm}^2$  BiOI -  $0.25 \text{ cm}^2$  BiVO<sub>4</sub> (active areas not aligned). **e**,  $0.315 (7 \times 0.045) \text{ cm}^2$  BiOI -  $0.52 (8 \times 0.065) \text{ cm}^2$  BiVO<sub>4</sub> (larger BiVO<sub>4</sub> area to account for scattered light). **f**,  $0.25 \text{ cm}^2$  BiOI -  $0.25 \text{ cm}^2$  BiVO<sub>4</sub> (active areas aligned). **g**, Simplified structure of the tandem device. The PEC tandem is irradiated from the transparent BiVO<sub>4</sub> side. **a,c,e,f**, CV traces under chopped, continuous and no light irradiation (**e, f**) correspond to the CV scans given in Fig. 3a from the main text). **b,d**, Chronoamperometry at 0 V bias under chopped light irradiation (AM 1.5G,  $100 \text{ mW cm}^{-2}$ , in 0.1 M KBi, 0.1 M K<sub>2</sub>SO<sub>4</sub>, pH 8.50, under N<sub>2</sub>). The results highlight the light scattering effect of BiVO<sub>4</sub>, as the devices with aligned (**a, b**) and misaligned pixels (**c, d**) display similar initial photocurrent densities of around 30-35  $\mu\text{A cm}^{-2}$ . Lateral scattering of light through the nanostructured BiVO<sub>4</sub> photoanode causes a decrease in the light intensity of direct irradiation, while the resulting diffuse irradiation is beneficial in case of the misaligned pixels, as depicted in Supplementary Fig. 21. A smaller portion of diffuse light is lost in case of the larger  $0.25 \text{ cm}^2$  BiOI -  $0.25 \text{ cm}^2$  BiVO<sub>4</sub> one-pixel devices, hence a higher initial photocurrent density of  $\approx 60 \mu\text{A cm}^{-2}$  is observed in that case (see **f** and Fig. 3b, main text).

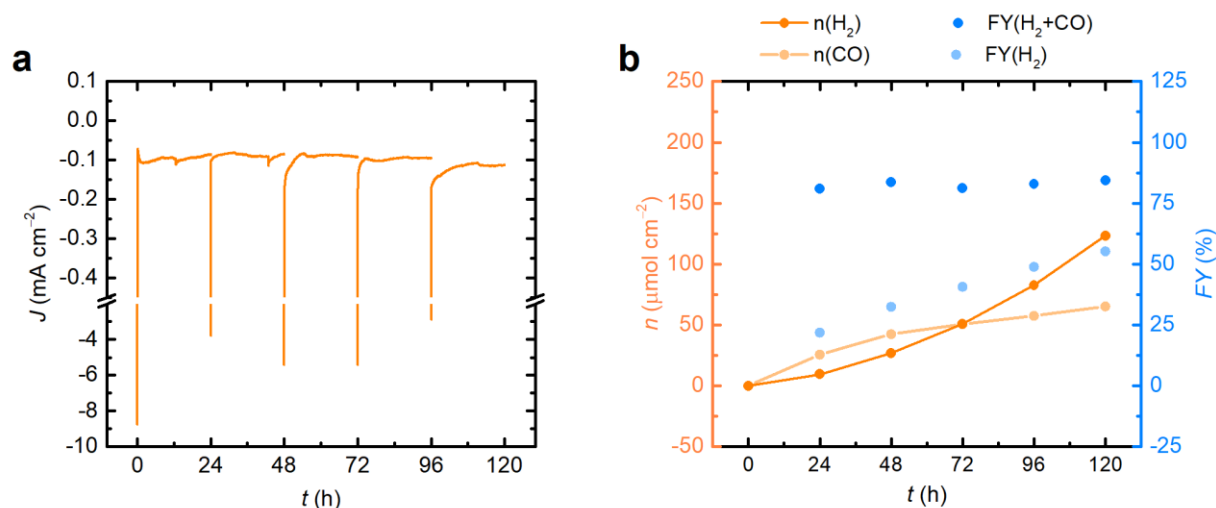


**Supplementary Fig. 21 | Light scattering within BiOI|GE|Pt - BiVO<sub>4</sub> devices of different configurations.**

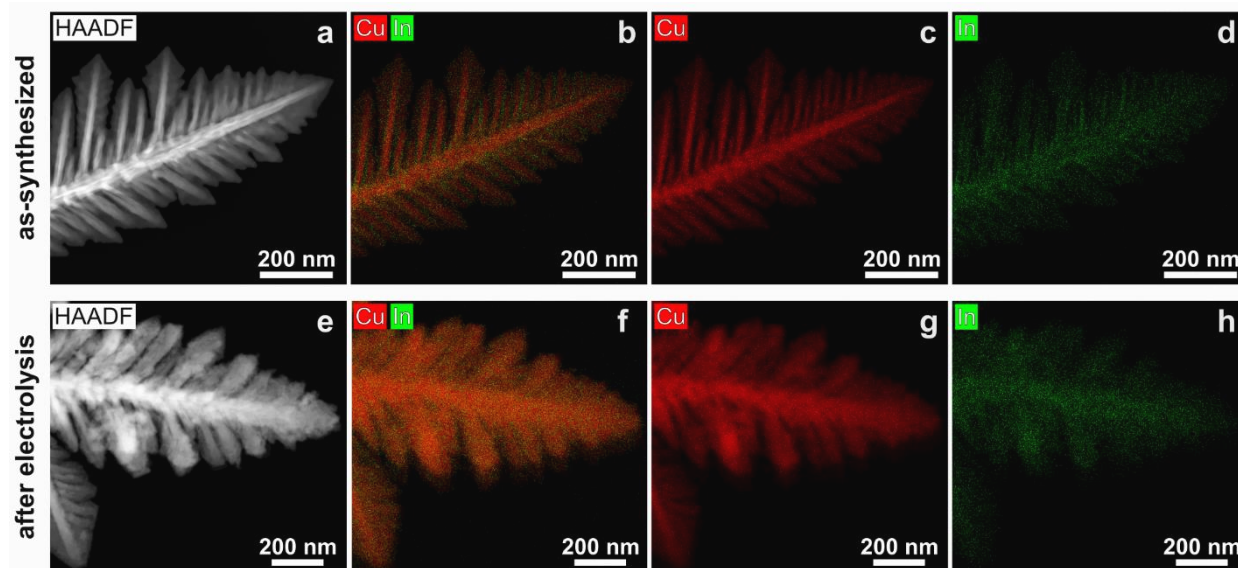
**a**, Beams of light remain parallel in the absence of scattering, i.e. the light intensity remains homogeneous over the entire active area. Optical losses are mainly caused by light absorption through the BiVO<sub>4</sub> layer and the two glass substrates. **b**, Light scattering over a wider area, corresponding to a 0.25 cm<sup>2</sup> BiOI - 0.25 cm<sup>2</sup> BiVO<sub>4</sub> tandem (Supplementary Fig. 20f). The light intensity is lowered around the edges of the BiVO<sub>4</sub> pixel, leading to additional optical losses. The homogeneous irradiation towards the centre consists of both scattered and direct light. **c**, Light scattering over a narrower pixel, as occurring in a 0.27 (6×0.045) cm<sup>2</sup> BiOI - 0.27 (6×0.045) cm<sup>2</sup> BiVO<sub>4</sub> tandem (Supplementary Fig. 20a,b). The area of homogeneous irradiation is relatively smaller, increasing optical losses. This qualitative assessment is supported by the observed photocurrents, as a single-pixel 0.25 cm<sup>2</sup> BiOI - 0.25 cm<sup>2</sup> BiVO<sub>4</sub> device provided a higher initial photocurrent at no applied bias (Fig. 3a,b) than multiple-pixel devices with equivalent BiVO<sub>4</sub> active areas (Supplementary Fig. 20b,d). Hence, light scattering through BiVO<sub>4</sub> plays a smaller role in case of larger pixel areas. **d**, Optical losses can be mitigated by assembling devices with an increased BiVO<sub>4</sub> area (e.g. the 0.315 (7×0.045) cm<sup>2</sup> BiOI - 0.52 (8×0.065) cm<sup>2</sup> BiVO<sub>4</sub> tandem from Supplementary Fig. 20e), which compensates for light scattering in several ways. The increased BiVO<sub>4</sub> pixel area (0.065 cm<sup>2</sup>) enables a more homogeneous irradiation of the photoactive BiOI area (defined by the grey Cr|Ag contact in **d**). A larger BiVO<sub>4</sub> photoanode also provides a higher absolute photocurrent, which improves the photocurrent overlap with the BiOI photocathode (see Supplementary Fig. 22). **e**, Scattering can also increase the photocurrent of misaligned pixels, as exemplified by the 0.225 (5×0.045) cm<sup>2</sup> BiOI - 0.25 cm<sup>2</sup> BiVO<sub>4</sub> device in Supplementary Fig. 20c,d.



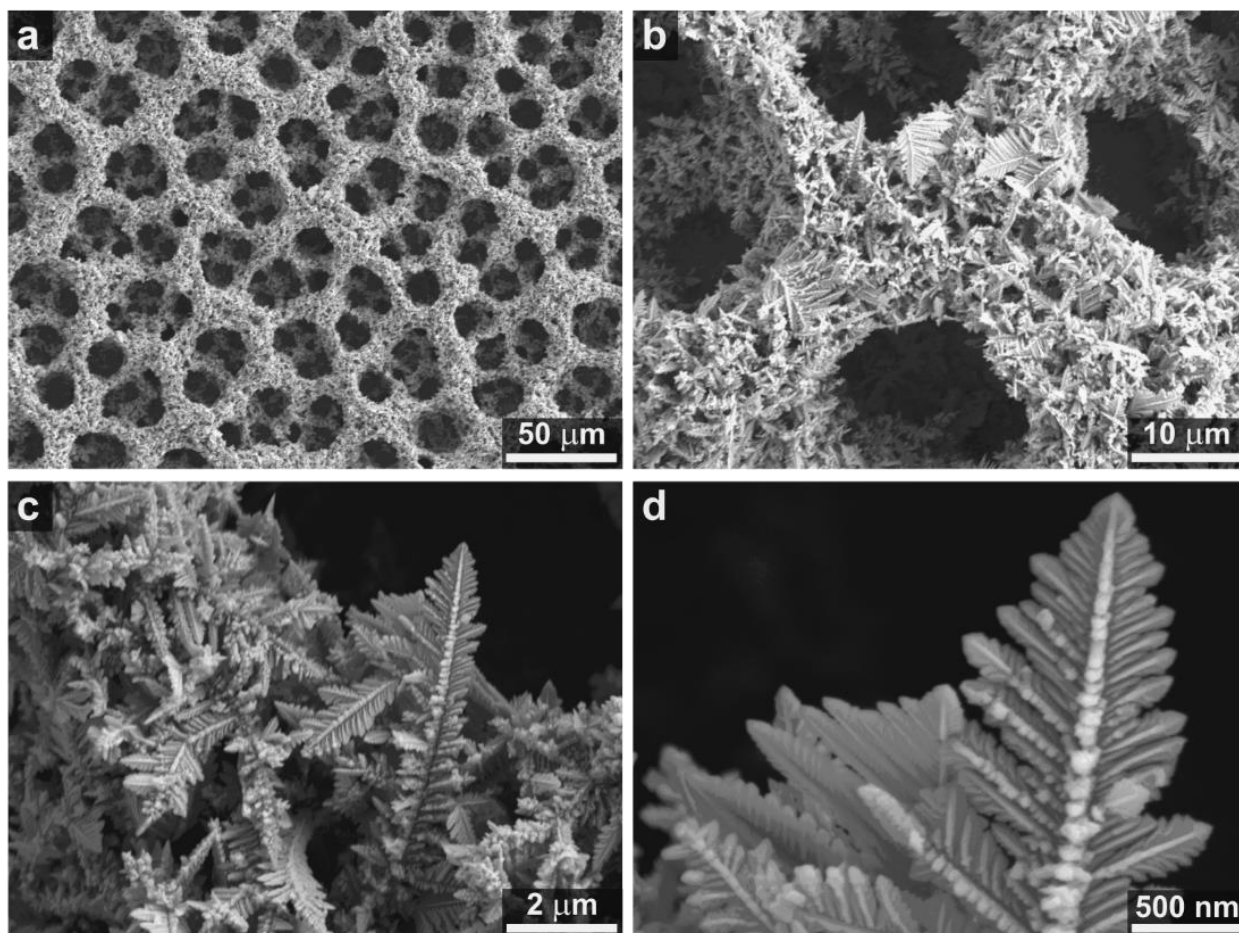
**Supplementary Fig. 22 | Overlap of the BiOI|GE|Pt and BiVO<sub>4</sub> photoelectrode currents.** Cyclic voltammetry (CV) scans of a photocathode consisting of seven  $0.045 \text{ cm}^2$  working BiOI pixels and a masked BiVO<sub>4</sub> photoanode with a  $0.52 (8 \times 0.065) \text{ cm}^2$  active area under chopped, continuous and no light irradiation (AM 1.5G,  $100 \text{ mW cm}^{-2}$ , in  $0.1 \text{ M KBi}$ ,  $0.1 \text{ M K}_2\text{SO}_4$ , pH 8.50, under  $\text{N}_2$ ). The overlap of the CV scans indicates that a BiOI-BiVO<sub>4</sub> tandem device can perform unassisted water splitting. In this case, the overlap occurs at  $\sim 0.55 \text{ V vs. RHE}$ , presenting a  $\sim 0.15 \text{ V}$  cathodic shift from the BiOI onset potential at  $\sim 0.7 \text{ V vs. RHE}$ . This applied potential is simulated during the stability test from Fig. 1h (main text), where a  $0.55 \text{ V}$  bias is applied to a BiOI PV device with a  $\sim 0.7 \text{ V } V_{\text{oc}}$ .



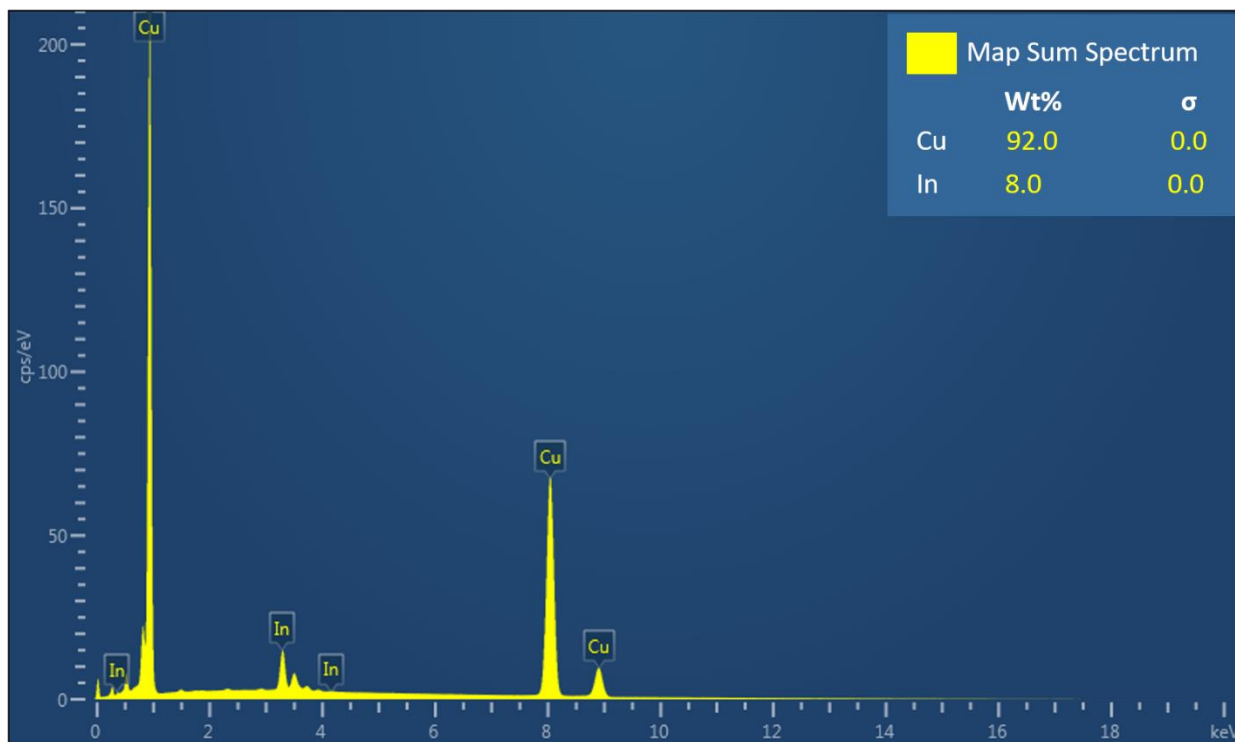
**Supplementary Fig. 23 | Long-term stability tests of the nanostructured Cu<sub>92</sub>In<sub>8</sub> alloy catalyst for electrochemical CO<sub>2</sub> reduction.** **a**, Long-term chronoamperometric trace, recorded at -0.3 V vs. RHE, in a 0.5 M KHCO<sub>3</sub> solution, under CO<sub>2</sub>. The electrochemical cell was re-purged with CO<sub>2</sub> every 24 h. **b**, Cumulative product amounts and faradaic yields. A decrease in the rate of CO production is observed after 72 h, while the rate of H<sub>2</sub> production is gradually increasing. The experiments were performed at room temperature.



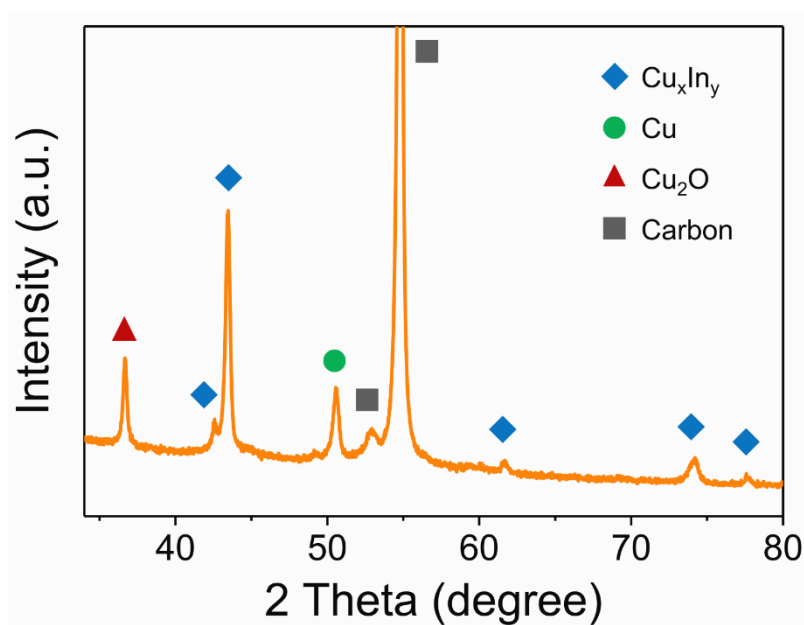
**Supplementary Fig. 24 | Pre- and post-catalysis HAADF and STEM mapping of the Cu<sub>92</sub>In<sub>8</sub> alloy electrocatalyst.** **a,e**, High-angle annular dark-field (HAADF) images. **b-d,f-h**, Scanning transmission electron microscopy (STEM) elemental mapping depicting overall (**b,f**), copper (**c,g**) and indium (**d,h**) distributions. Data is obtained prior (**a-d**) and after (**e-h**) the long-term CO<sub>2</sub> reduction experiment described in Supplementary Fig. 23. The dendritic CuIn alloy undergoes an *in situ* phase transformation during operation where the In phase gradually migrates into the bulk of the dendrites. This process exposes the Cu phase on the catalyst surface, which is mainly active towards H<sub>2</sub> evolution under the experimental conditions<sup>5</sup>.



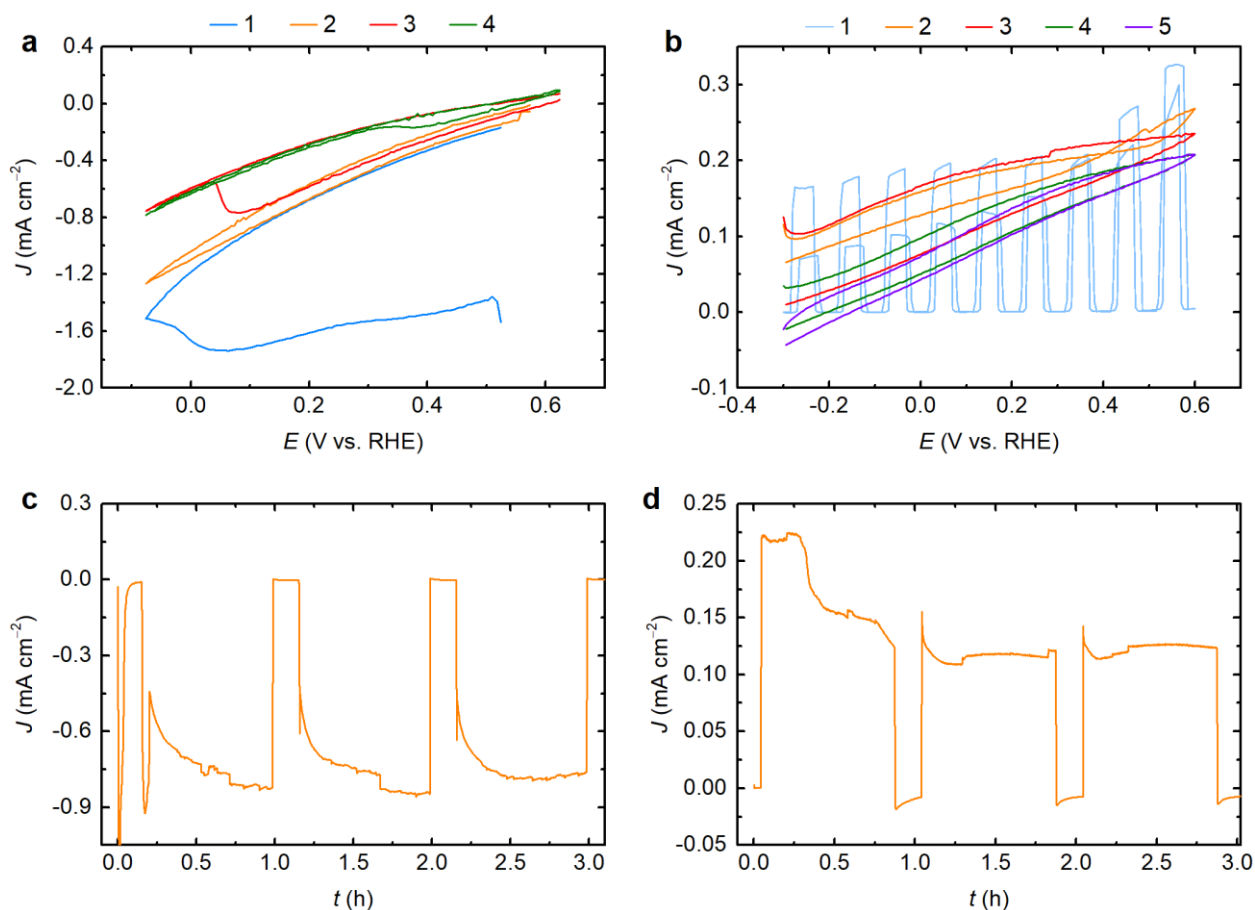
**Supplementary Fig. 25 | SEM and HR-SEM analysis of the  $\text{Cu}_{92}\text{In}_8$  alloy electrocatalyst at different magnifications. a-d,** The catalyst displays a dendritic foam morphology, which enables it to attain a high selectivity towards  $\text{CO}_2$  reduction at a low overpotential.



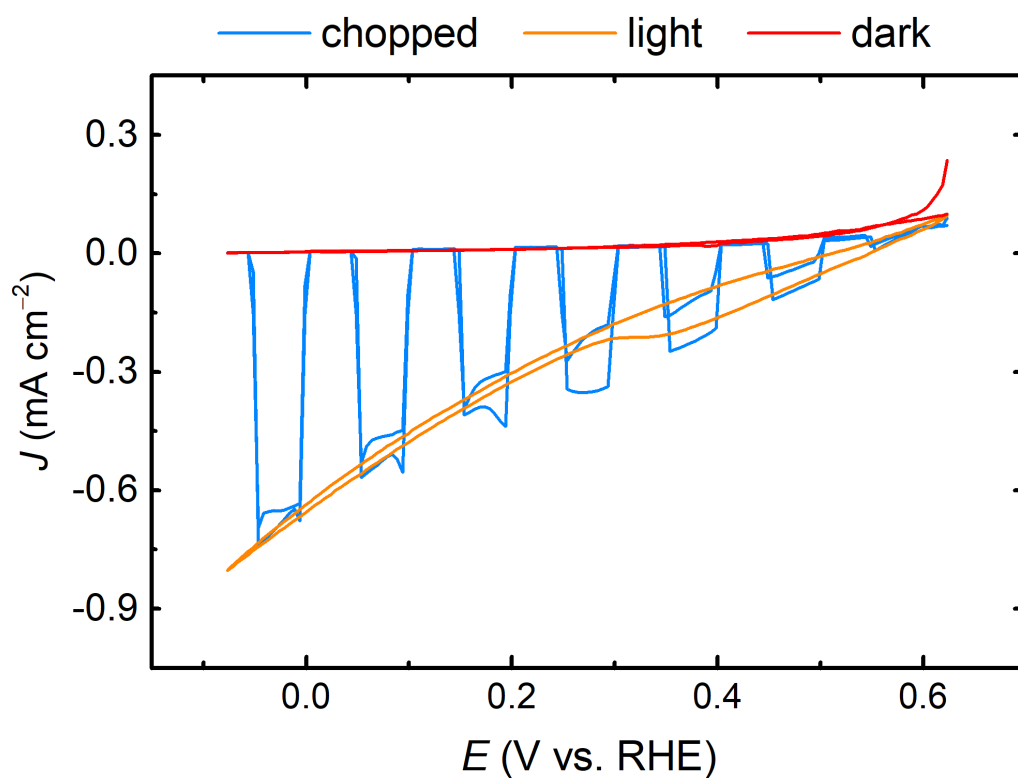
Supplementary Fig. 26 | EDX analysis confirms the composition of the  $\text{Cu}_{92}\text{In}_8$  alloy employed for  $\text{CO}_2$  reduction.



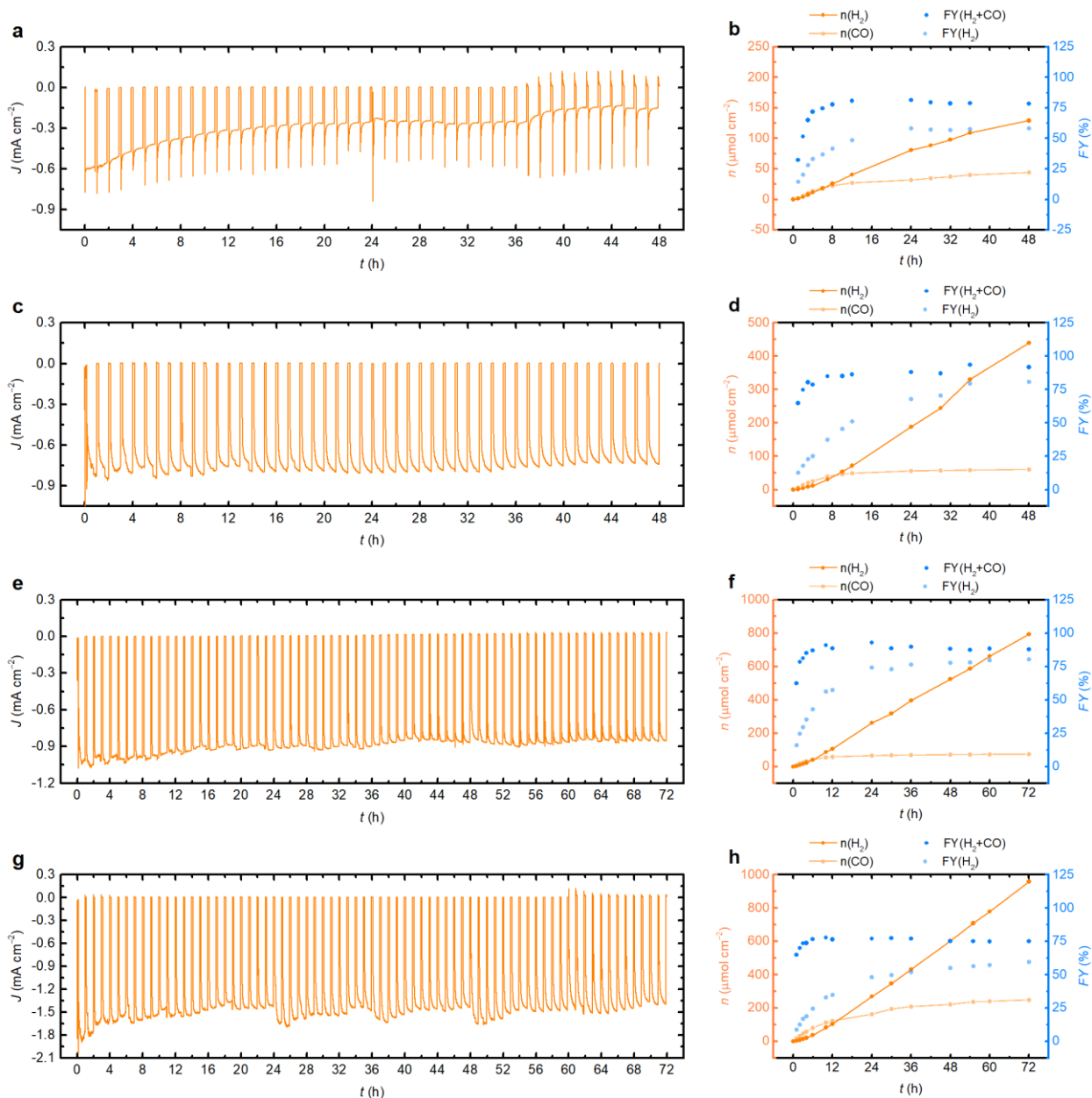
Supplementary Fig. 27 | XRD analysis of the  $\text{Cu}_{92}\text{In}_8$  alloy catalyst shows  $\text{Cu}_x\text{In}_y$  alloy peaks along with some residual Cu and  $\text{Cu}_2\text{O}$  components.  $\text{Cu}_2\text{O}$  appears due to aerial oxidation and is reduced back to metallic Cu under operation (see Supplementary Fig. 28). JCPDS files: 42-1476 and 35-1150 for  $\text{Cu}_x\text{In}_y$  alloy, 85-1326 for Cu, and 75-1531 for  $\text{Cu}_2\text{O}$  were used to assign the peaks.



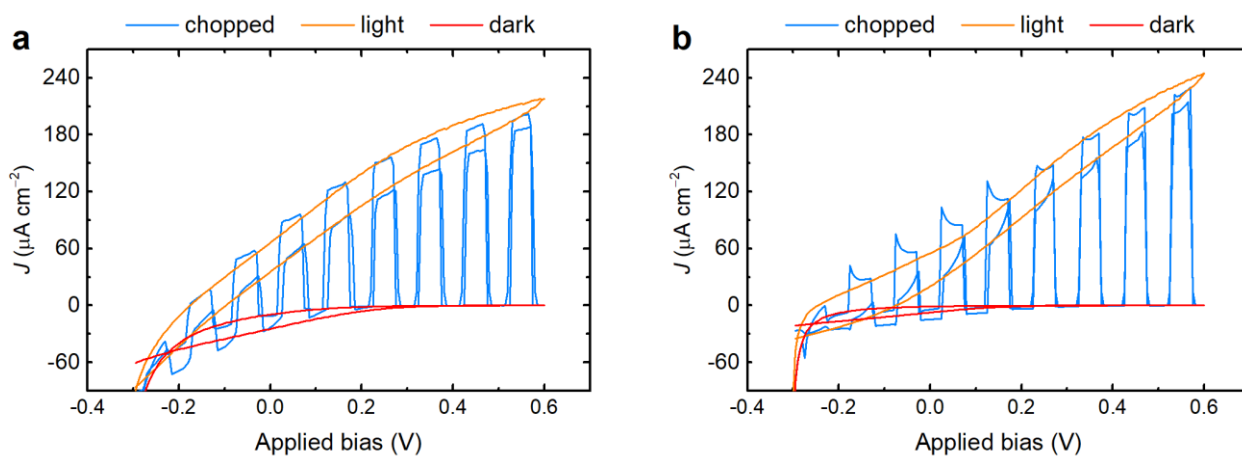
**Supplementary Fig. 28 | Reduction of the  $\text{Cu}_2\text{O}$  phase from the  $\text{Cu}_{92}\text{In}_8$  catalyst surface during PEC operation.** **a,c**,  $\text{BiOI}|\text{GE}|\text{Cu}_{92}\text{In}_8$  photocathodes. **b,d**,  $\text{BiOI}|\text{GE}|\text{Cu}_{92}\text{In}_8 - \text{BiVO}_4$  tandem devices. Due to an aerial oxidation, a minor  $\text{Cu(I)}$  oxide phase ( $\text{Cu}_2\text{O}$ ) appears on the nanodendritic catalyst surface (see Supplementary Fig. 27). Under photoelectrochemical conditions, this oxide layer is rapidly reduced back to metallic  $\text{Cu}$ . Thus, during operation, the active catalyst is pure metallic  $\text{Cu}_{92}\text{In}_8$  alloy which does not contain any oxide component. This oxide reduction can be observed through an increased photocurrent in the cyclic voltammograms of the photocathodes and tandem devices which disappears after 3-5 cycles (**a,b**), or through a high initial photocurrent within the first 30 min in chronoamperometry, before reaching steady state (**c,d**).



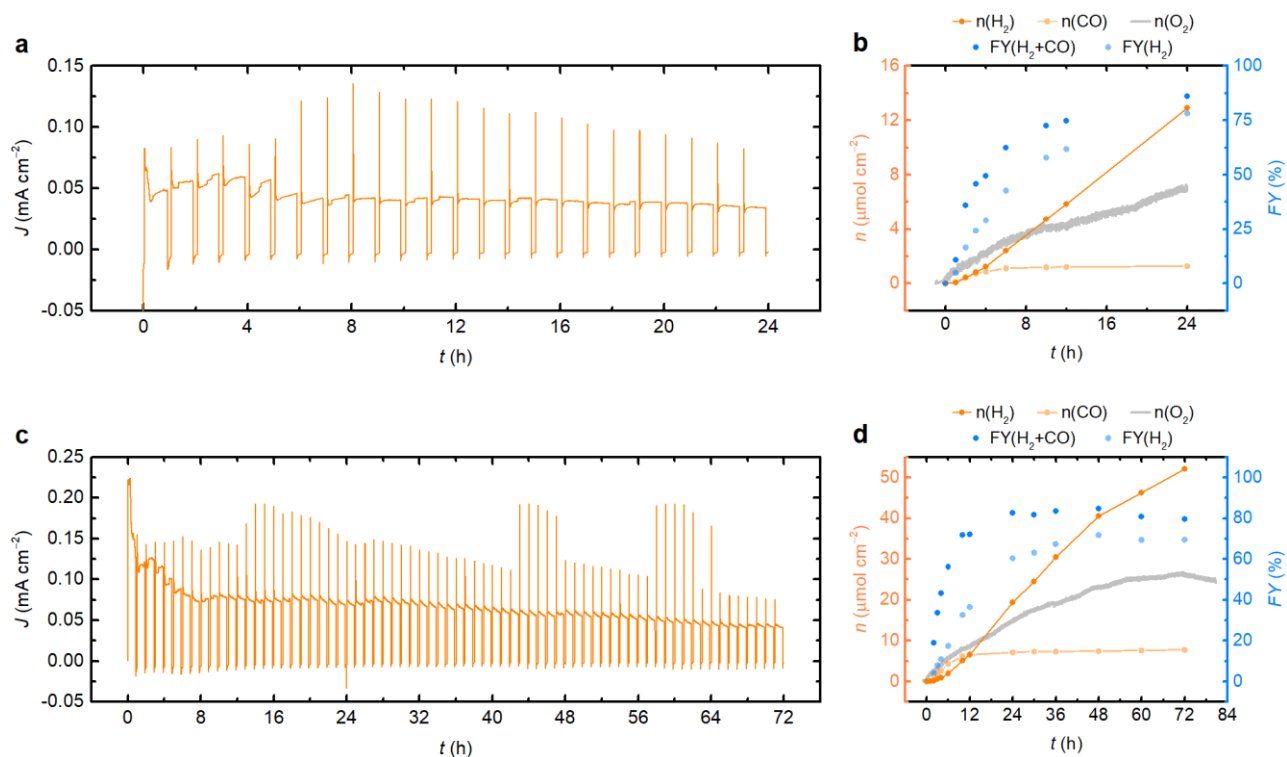
**Supplementary Fig. 29** | Cyclic voltammetry scans of a 0.27 (6×0.045) cm<sup>2</sup> BiOI|GE|Cu<sub>92</sub>In<sub>8</sub> photocathode for CO<sub>2</sub> reduction, under chopped, continuous and no light irradiation. Light experiments are performed under 1 sun irradiation (AM1.5G, 100 mW cm<sup>-2</sup>), in a 0.5 M KHCO<sub>3</sub> electrolyte solution, under CO<sub>2</sub>, pH 7.4.



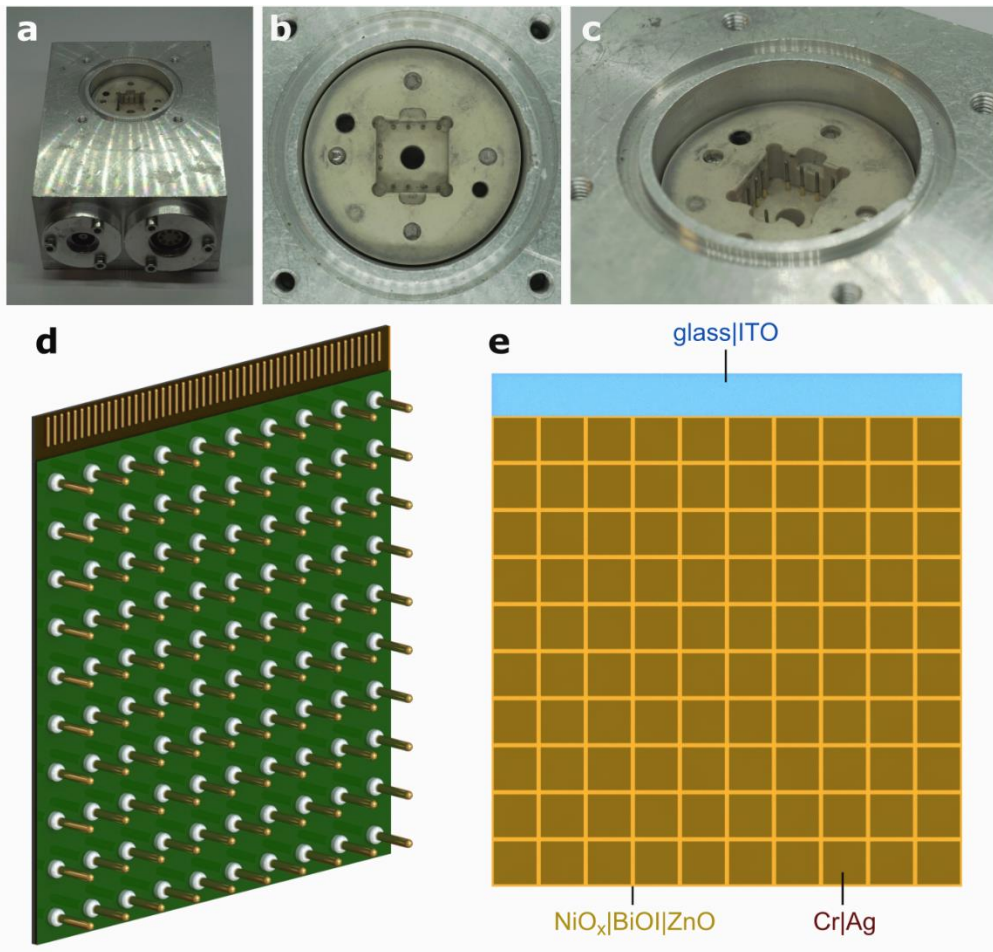
**Supplementary Fig. 30 | Performance of BiOI|GE|Cu<sub>92</sub>In<sub>8</sub> photocathodes towards CO<sub>2</sub> reduction. a,c,e,g,** Evolution of the photocurrent over time at an applied potential of 0 V vs. RHE. **b,d,f,h,** Cumulative amounts of products and faradaic yields. **a,b,** 0.27 (6×0.045) cm<sup>2</sup> BiOI photocathode - CV scans are performed before the long-term tests (Supplementary Fig. 29); electrolyte is replaced and purged with CO<sub>2</sub> after 24 h. **c,d,** 0.18 (4×0.045) cm<sup>2</sup> and **e,f,** 0.27 (6×0.045) cm<sup>2</sup> BiOI photocathodes - no initial CVs are performed; the PEC cells remain sealed throughout the experiment. **g,h,** 0.36 (8×0.045) cm<sup>2</sup> BiOI photocathode - no initial CVs are performed; the sealed PEC cell is re-purged with CO<sub>2</sub> after every 24 h without replacing the electrolyte. Tests were performed under 1 sun irradiation (AM 1.5G, 100 mW cm<sup>-2</sup>) in a 0.5 M KHCO<sub>3</sub> solution, pH 7.4, under CO<sub>2</sub>, at room temperature. The photocathodes tested without performing initial CVs display a high initial selectivity towards CO<sub>2</sub> reduction, reaching a CO:H<sub>2</sub> ratio of up to 6.38:1 after 1 h of chronoamperometry (**h**). In every case, the nanostructured Cu<sub>92</sub>In<sub>8</sub> catalyst displays a decreased activity towards CO formation after the first 24 h of operation, which may be traced back to the changes in current and applied voltage caused by light chopping.



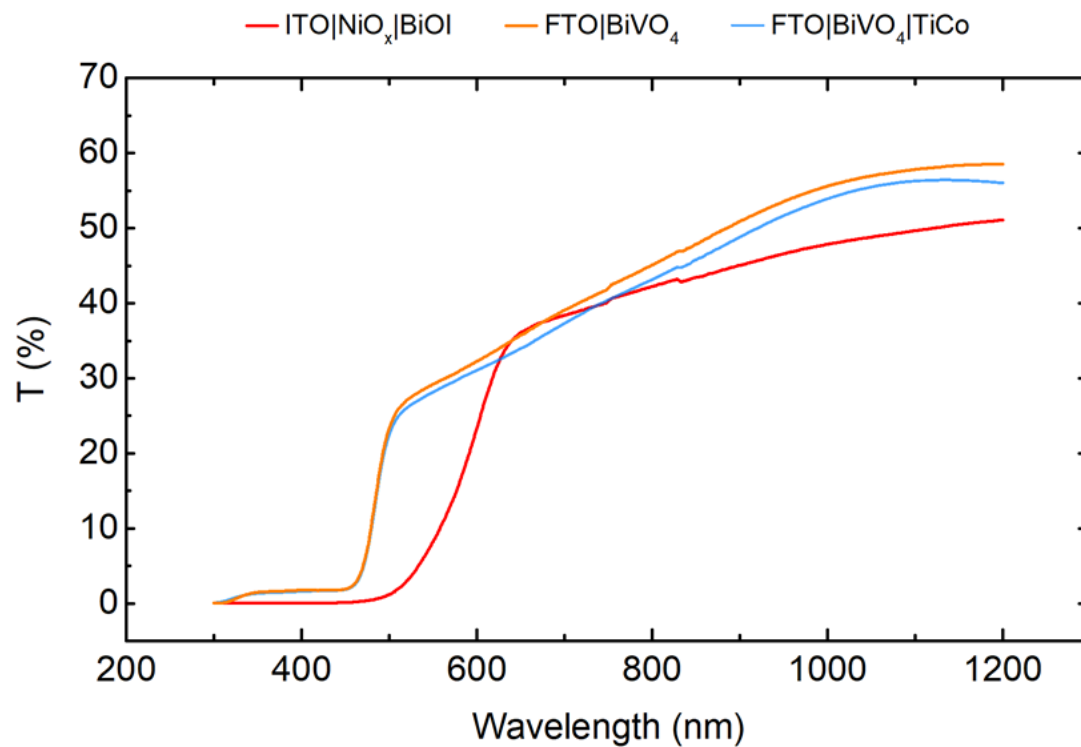
**Supplementary Fig. 31 | CV scans of a  $0.315 (7 \times 0.045) \text{ cm}^2 \text{ BiOI} | \text{GE} | \text{Cu}_{92}\text{In}_8 - 0.52 (8 \times 0.065) \text{ cm}^2 \text{ BiVO}_4$  PEC tandem device for  $\text{CO}_2$  reduction coupled to  $\text{O}_2$  evolution, under chopped, continuous and no light irradiation. **a**, Before the stability test. **b**, After 24 h chronoamperometry at 0 V applied bias (Supplementary Fig. 32a). Light tests are performed under 1 sun (AM1.5G,  $100 \text{ mW cm}^{-2}$ ), in 0.5 M  $\text{KHCO}_3$ , under  $\text{CO}_2$ , pH 7.4.**



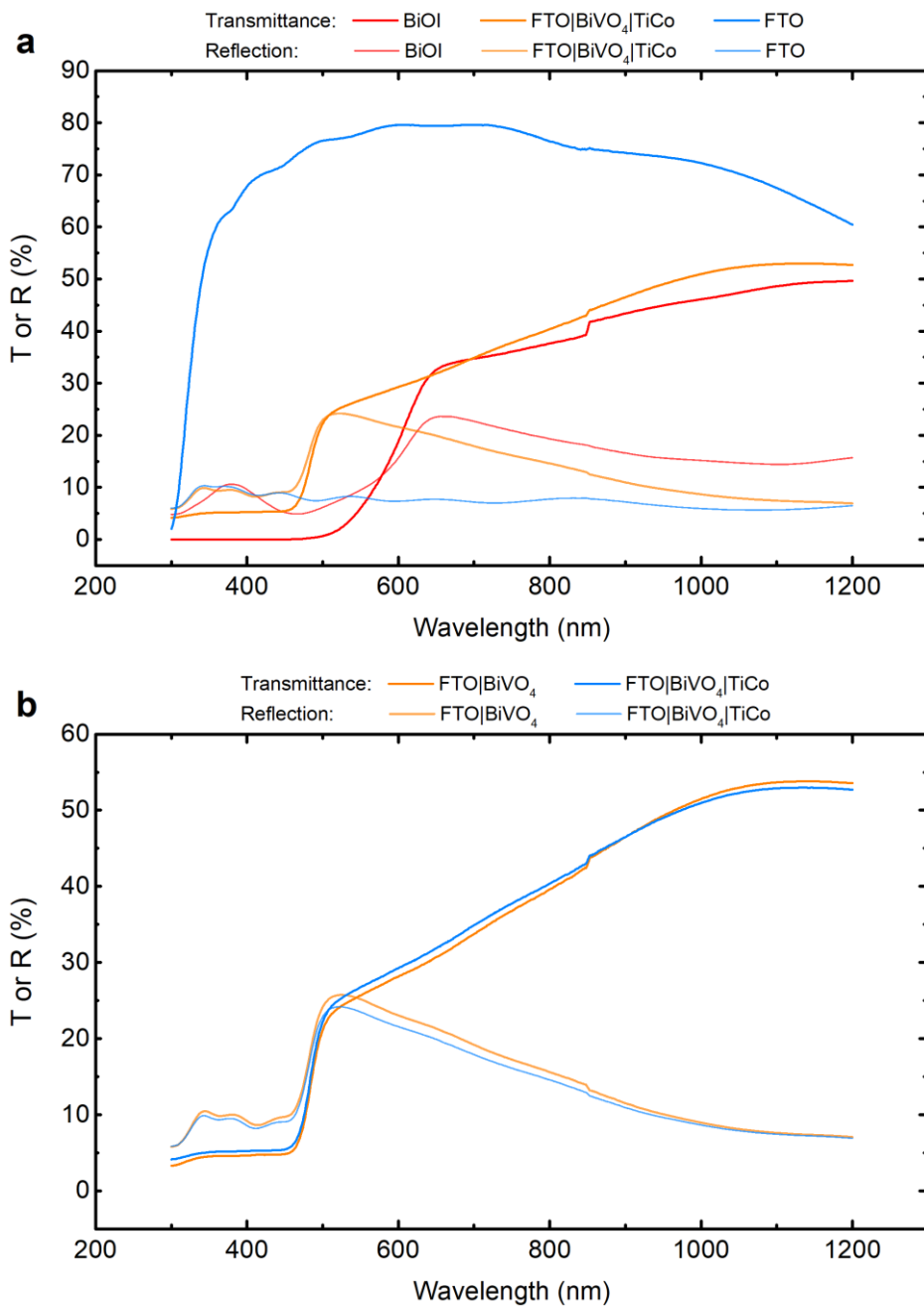
**Supplementary Fig. 32 | Performance of BiOI|GE|Cu<sub>92</sub>In<sub>8</sub> - BiVO<sub>4</sub> tandem devices towards unassisted CO<sub>2</sub> reduction coupled to O<sub>2</sub> evolution. **a,c**, Evolution of the photocurrent over time at 0 V applied bias. **b,d**, Amounts of products and corresponding faradaic yields. **a,b**, 0.315 (7×0.045) cm<sup>2</sup> BiOI|GE|Cu<sub>92</sub>In<sub>8</sub> - 0.52 (8×0.065) cm<sup>2</sup> BiVO<sub>4</sub> PEC tandem - CV scans are performed before the long-term tests (Supplementary Fig. 31a). **c,d**, 0.225 (5×0.045) cm<sup>2</sup> BiOI|GE|Cu<sub>92</sub>In<sub>8</sub> - 0.52 (8×0.065) cm<sup>2</sup> BiVO<sub>4</sub> PEC tandem - no initial CVs are performed. The PEC cells remain sealed throughout the experiment in both cases. As observed earlier for the photocathodes, a higher initial CO:H<sub>2</sub> ratio (3.72:1 after 2 h of CA) is achieved in the absence of initial CVs, whereas the electrocatalyst activity diminishes over the first 24 h due to current and voltage fluctuations induced by light chopping. Experiments were performed under chopped irradiation (AM 1.5G, 100 mW cm<sup>-2</sup>, 50 min on, 10 min off cycles) in a 0.5 M KHCO<sub>3</sub> solution, pH 7.4, under CO<sub>2</sub>, at room temperature.**



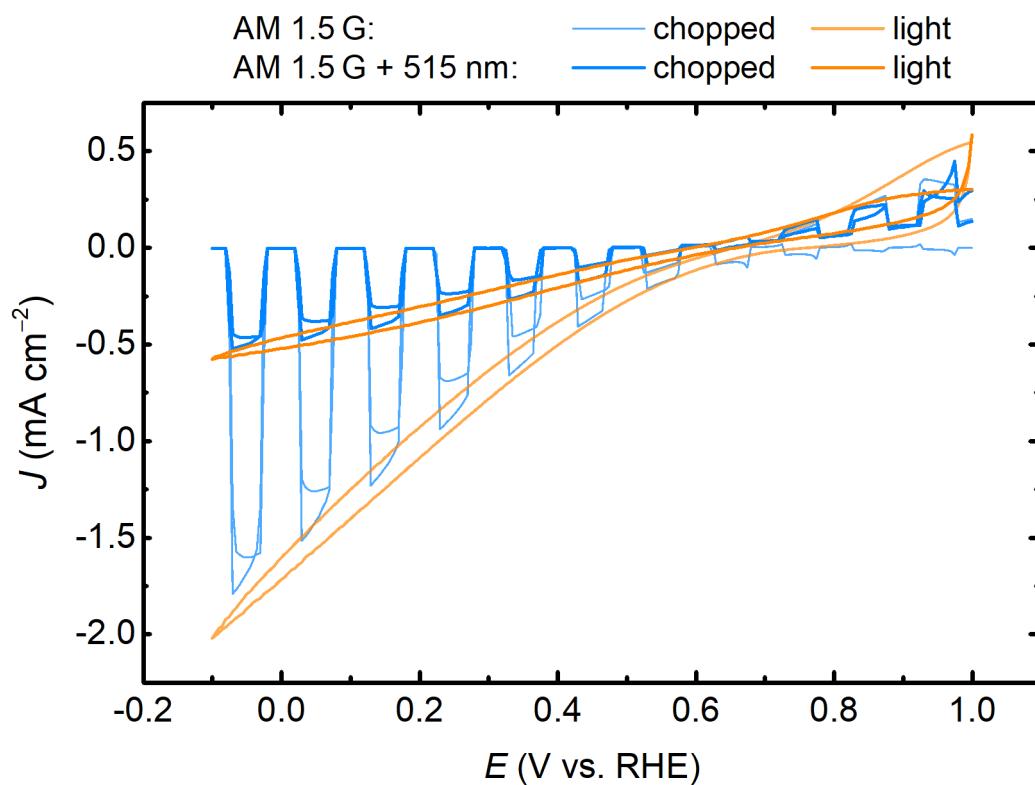
**Supplementary Fig. 33 | Manufacturing and characterisation of multiple-pixel PV devices on a large scale.** **a,b,c**, Photographs of an 8-pin sample holder employed to measure  $J$ - $V$  curves of small-scale, 8-pixel devices. Each individual pin can be connected to a separate current-voltage meter, hence multiple pixels can in principle be recorded in parallel. A similar arrangement can be envisioned on a larger scale, as proposed next. **d**, Depiction of a 100-pin sample holder, which could simultaneously probe all pixels on a larger device. In that case, the quality of each pixel can be assessed by  $J$ - $V$  curves, or by comparing the open circuit voltage against a threshold. The  $10 \times 10$  array of pins could be fabricated onto printed circuit boards, mimicking the designs encountered for processor chips. **e**, Corresponding schematic of a large-scale, 100-pixel device. An array of pixels can be simply deposited by evaporating the top metal contact through a shadow mask, defining the pixel size and density. In large scale manufacturing, pixels could be placed closer to each other, minimizing the non-active areas. Hence, the multiple pixel-design does not introduce any significant challenges in terms of scalability compared to conventional single-pixel approaches.



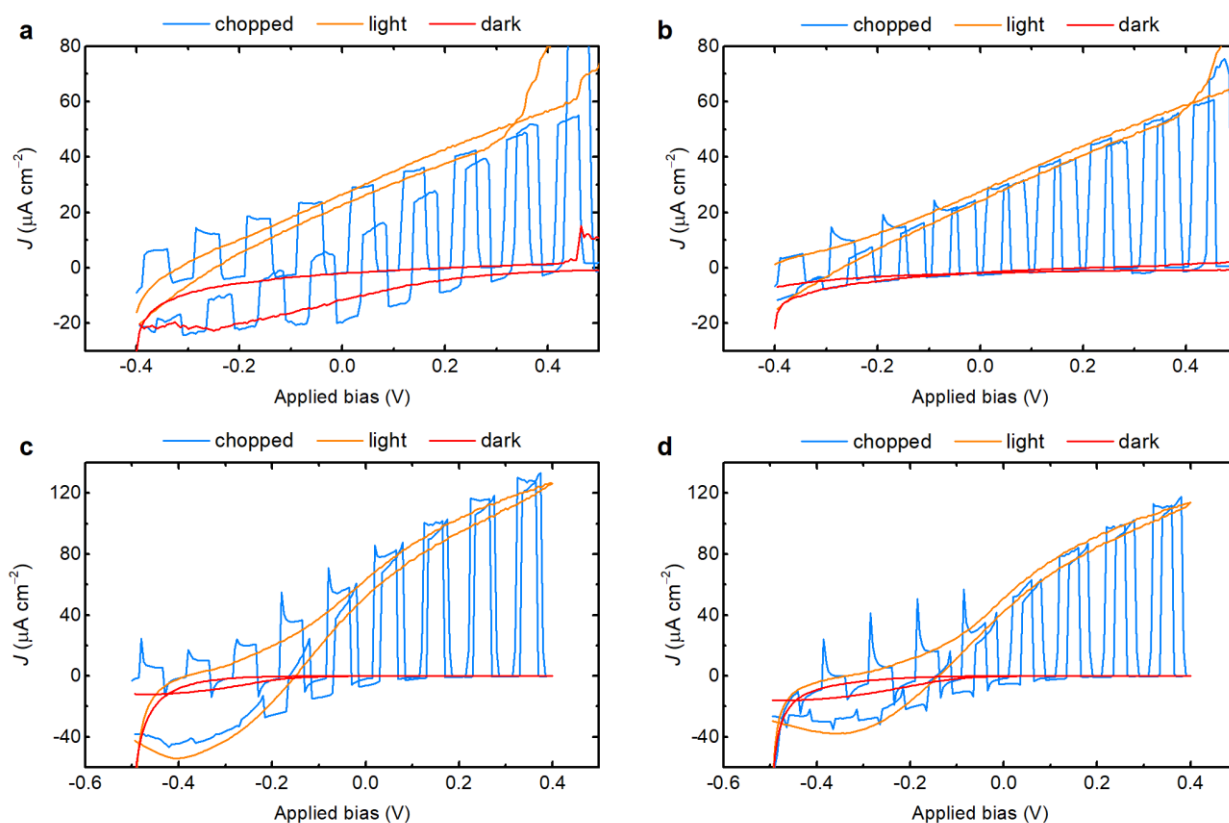
**Supplementary Fig. 34 | UV-vis transmittance spectra of BiOI and BiVO<sub>4</sub>.** The front BiVO<sub>4</sub> photoanode can absorb light up to 500 nm, leaving a small part of the solar spectrum available for the BiOI light absorber. The thin, transparent TiCo water oxidation catalyst does not have a significant effect on the transparency of the BiVO<sub>4</sub> photoanode.



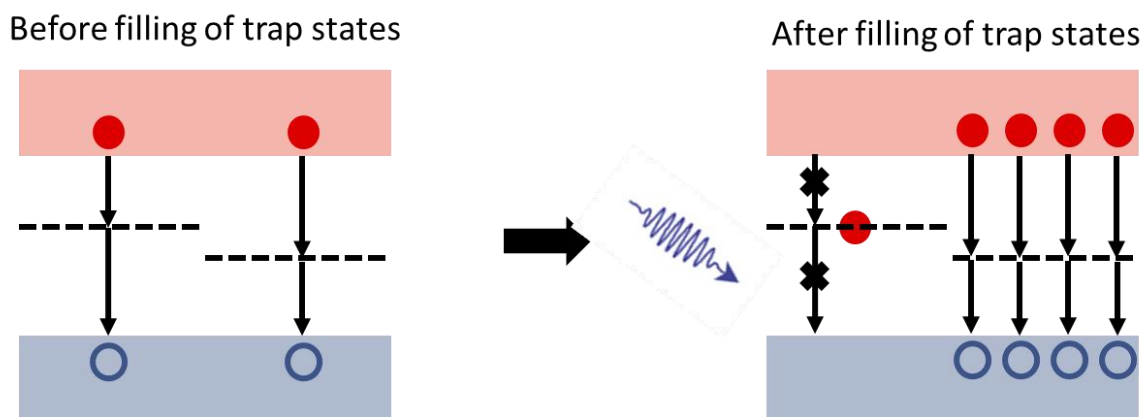
**Supplementary Fig. 35 | UV-vis transmittance and reflection spectra of FTO substrates, BiOI and BiVO<sub>4</sub>.**  
**a**, Spectra of BiOI, BiVO<sub>4</sub>|TiCo and FTO. **b**, Comparison between the spectra of BiVO<sub>4</sub> with or without the TiCo water oxidation catalyst. Besides the overlap in their absorption ranges, the two light absorbers are also light scattering. Combined with the transmittance losses from the transparent glass substrates (i.e. FTO), this explains the low photocurrents observed in PEC experiments. The grating and detector change at 850 nm causes a small deviation in the transmittance and reflection spectra. All samples are measured through substrate (glass) slide first.



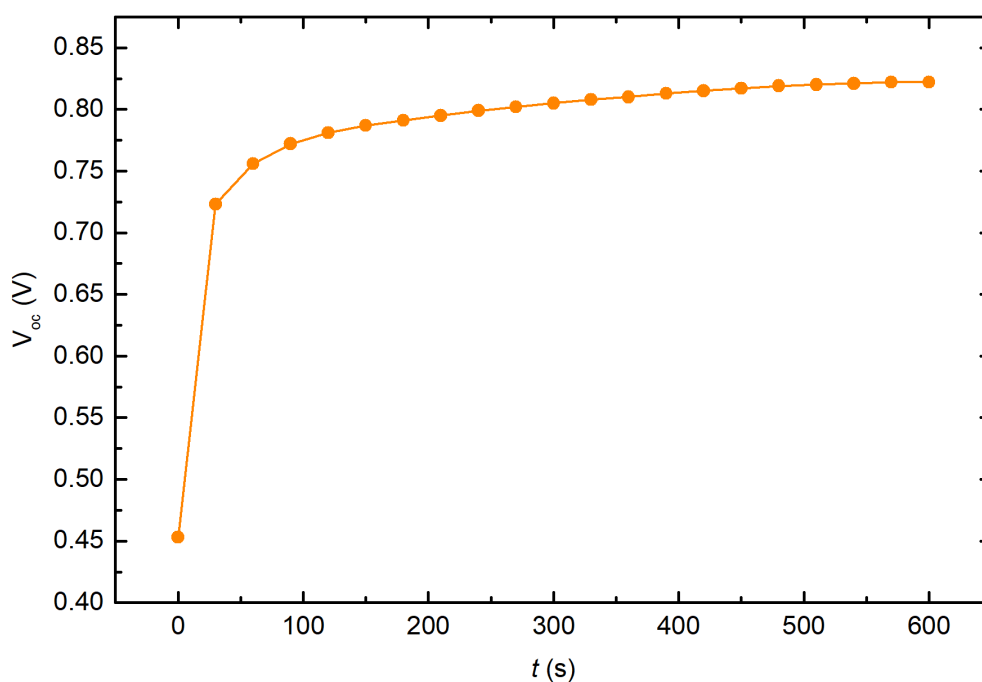
**Supplementary Fig. 36 | CVs of a BiOI|GE|Pt photocathode.** Measured under 1 sun irradiation (AM 1.5G,  $100 \text{ mW cm}^{-2}$ , in  $0.1 \text{ M KBi}$ ,  $0.1 \text{ M K}_2\text{SO}_4$ , pH 8.50, under  $\text{N}_2$ ), with or without a 515 nm cut-off filter. The 515 nm light filtering results in significantly lower photocurrent densities, which resemble the photocurrents displayed by tandem devices (i.e. with BiOI behind  $\text{BiVO}_4$ ).



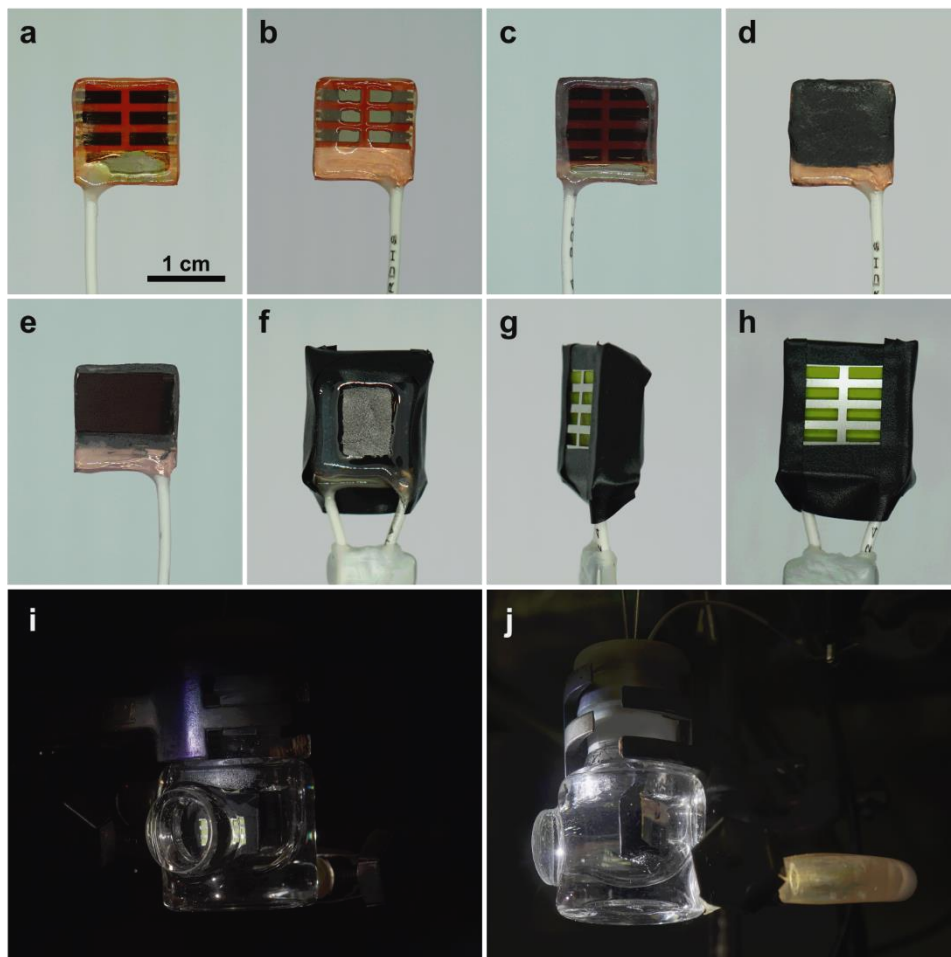
**Supplementary Fig. 37 | Trap filling behavior of the BiOI|GE|Pt - BiVO<sub>4</sub> tandem devices during operation. a,b**, CVs of a 0.225 (5×0.045) cm<sup>2</sup> BiOI - 0.25 cm<sup>2</sup> BiVO<sub>4</sub> tandem recorded before (a) and after (b) 12 h chronoamperometry (CA) at 0 V applied bias. **c,d**, CVs of a 0.25 cm<sup>2</sup> BiOI - 0.25 cm<sup>2</sup> BiVO<sub>4</sub> tandem recorded before (c) and after (d) 12 h CA. Instead of promoting device degradation, the prolonged light exposure leads to a decrease in the dark current (b, d) and an increase of the device photovoltage (see earlier onset voltage for water splitting in b). This may be explained by a trap filling mechanism, which manifests through an increase in V<sub>oc</sub> during light soaking of the devices (see Supplementary Fig. 39). Experiments are performed under simulated 1 sun irradiation (AM 1.5G, 100 mW cm<sup>-2</sup>), in 0.1 M KBi, 0.1 M K<sub>2</sub>SO<sub>4</sub>, pH 8.50, under N<sub>2</sub>.



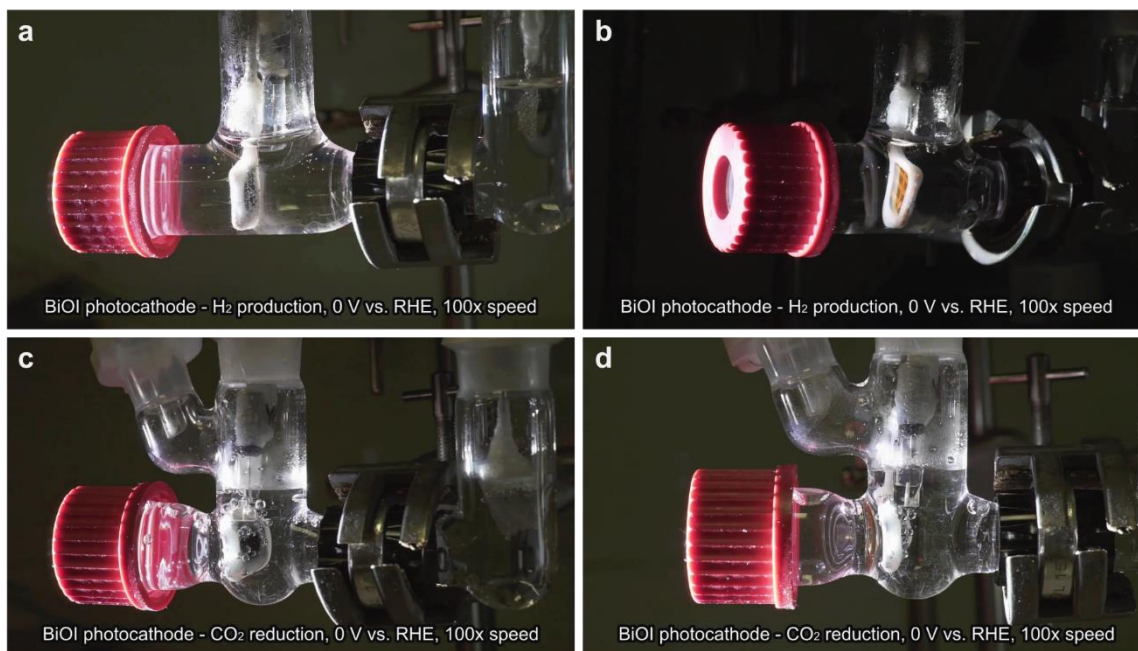
**Supplementary Fig. 38 | Schematic showing the effect of light soaking on the recombination kinetics.** Before prolonged light exposure all defect states are unoccupied (left part). After prolonged light exposure trap states are filled (right part) reducing the recombination rate, increasing the carrier density, and open circuit voltage.



**Supplementary Fig. 39 | Light soaking effect on the photovoltage of BiOI PV devices.** In this case, the  $V_{oc}$  of a  $0.045 \text{ cm}^2$  PV device is increasing from 0.45 V to above 0.8 V over the course of 10 minutes. This increase in the PV open circuit voltage is reflected in the PEC onset potential (see Supplementary Fig. 37), as both correspond to the conditions of no current flow.



**Supplementary Fig. 40 | Photographs of the BiOI devices during encapsulation and operation. a-e,** Intermediate steps in the BiOI photocathode encapsulation: **a,b** - wiring and insulating the active areas using epoxy resin; **c,d** - applying the graphite epoxy paste as conductive encapsulant; **e** - attachment of a Cu foil with a dendritic  $\text{Cu}_{92}\text{In}_8$  foam catalyst onto the fresh graphite paste. **f,g,h**, Close-up images of the masked  $0.315 (7 \times 0.045) \text{ cm}^2$  BiOI -  $0.52 (8 \times 0.065) \text{ cm}^2$   $\text{BiVO}_4$  tandem device. **i,j**, Photographs of the wired tandem device under operation in a one-compartment PEC cell.



**Supplementary Fig. 41 | Snapshots from Supplementary Movie 1 of BiOI photocathodes under operation in a three-electrode system. a,b**, Photocathodes with a Pt catalyst for H<sub>2</sub> evolution. **c,d**, Photocathodes with a Cu<sub>92</sub>In<sub>8</sub> catalyst for CO<sub>2</sub> reduction to syngas. The stability tests are performed at an applied potential of 0 V vs. RHE. The movie speed is increased to highlight the bubble formation.

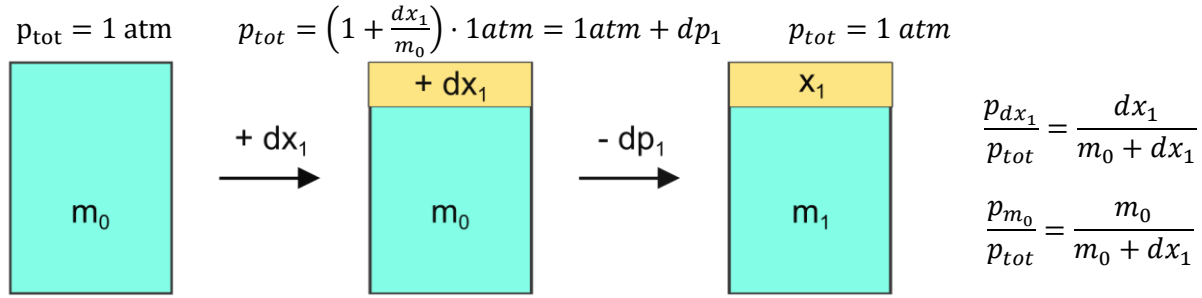
**Supplementary Movie 1 | H<sub>2</sub> and syngas production using BiOI photocathodes.** Details are given in the embedded video subtitles and in the caption of Supplementary Fig. 41.

**Supplementary Movie 2 | Degradation of unprotected BiOI photocathodes during CVs under chopped light irradiation.** Details are given in the movie subtitles and in the caption of Supplementary Fig. 15.

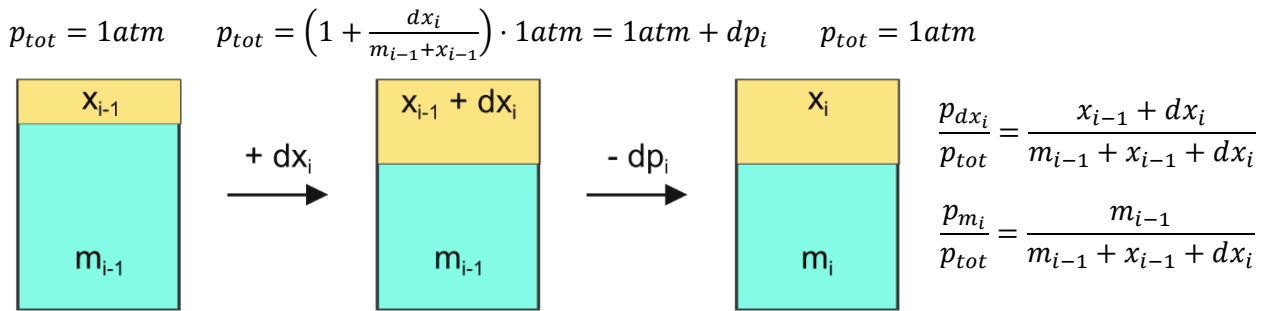
## Supplementary Discussion 1 | Generalized model for gas leakage correction.

The gas leakage model is based on a 2-component system. The chamber is initially filled with a known amount  $m_0$  of a reference gas, at atmospheric pressure ( $p_{tot} = 1 \text{ atm}$ ). A second gas is produced in the chamber in increments  $dx_i$ , amounting to an amount of  $x_i$  after  $i$  steps. In this model, every increment occurs in two sub steps. First, an amount of gas  $dx_i$  is produced in the chamber, increasing the total pressure. Then, the pressure returns to its original value through release of a gas mixture. This assumes that the two gases are evenly mixed and leak at the same relative rate.

Step 1:



Step  $i$ :



### Model for $\text{H}_2$ , CO

With  $m_i + x_i = m_0$  and  $\frac{m_i}{m_0} = \frac{p m_i}{p_{tot}}$ :

$$\frac{m_{i-1}}{m_0 + dx_i} = \frac{m_i}{m_0} = \left(\frac{[\text{CH}_4]_i}{[\text{CH}_4]_0}\right) = f_i(t)$$

( $f_i(t)$  is the fitting of the normalized  $\text{CH}_4$  signal decay as a function of time)

$$\frac{x_{i-1} + dx_i}{m_{i-1}} = \frac{x_i}{m_i} \Rightarrow dx_i = \left(\frac{x_i}{m_i} - \frac{x_{i-1}}{m_{i-1}}\right) \cdot m_{i-1} = \left(\frac{[\text{H}_2]_i}{[\text{CH}_4]_i} - \frac{[\text{H}_2]_{i-1}}{[\text{CH}_4]_{i-1}}\right) \cdot m_{i-1}$$

$$m_{i-1} = m_0 \cdot f_{i-1}(t) = m_0 \cdot \left(\frac{[\text{CH}_4]_{i-1}}{[\text{CH}_4]_0}\right) \Rightarrow dx_i = \left(\frac{[\text{H}_2]_i}{[\text{CH}_4]_i} - \frac{[\text{H}_2]_{i-1}}{[\text{CH}_4]_{i-1}}\right) \cdot m_0 \cdot \left(\frac{[\text{CH}_4]_{i-1}}{[\text{CH}_4]_0}\right)$$

### Model for $\text{O}_2$

$$\frac{x_{i-1} + dx_i}{m_{i-1}} = \frac{x_i}{m_i} \Rightarrow dx_i = \frac{m_{i-1}}{m_i} \cdot x_i - x_{i-1} = \frac{f_{i-1}(t)}{f_i(t)} \cdot x_i - x_{i-1}$$

## Supplementary References

1. Hoye, R. L. Z. *et al.* Improved Open- Circuit Voltage in ZnO – PbSe Quantum Dot Solar Cells by Understanding and Reducing Losses Arising from the ZnO Conduction Band Tail. *Adv. Energy Mater.* **4**, 1301544 (2014).
2. Hoye, R. L. Z. *et al.* Strongly enhanced photovoltaic performance and defect physics of air-stable bismuth oxyiodide (BiOI). *Adv. Mater.* **29**, 1702176 (2017).
3. Huq, T. N. *et al.* Electronic structure and optoelectronic properties of bismuth oxyiodide robust against percent-level iodine-, oxygen-, and bismuth-related surface defects. *Adv. Funct. Mater.* **30**, 1909983 (2020).
4. Pornrungrroj, C. *et al.* Bifunctional perovskite-BiVO<sub>4</sub> tandem devices for uninterrupted solar and electrocatalytic water splitting cycles. *Adv. Funct. Mater.* **31**, 2008182 (2020).
5. Rahaman, M. *et al.* Selective CO production from aqueous CO<sub>2</sub> using a Cu<sub>96</sub>In<sub>4</sub> catalyst and its integration into a bias free solar perovskite-BiVO<sub>4</sub> tandem device. *Energy Environ. Sci.* **13**, 3536–3543 (2020).